

國立臺灣大學理學院物理學研究所

碩士論文

Department of Physics

College of Science

National Taiwan University

Master Thesis



第一原理計算研究外爾和狄拉克半金屬 LaAlGe 和  
CuMnAs 之體光伏效應和量子幾何學

An *Ab Initio* Study of Bulk Photovoltaic Effect and its  
Quantum Geometry in Weyl and Dirac Semimetal LaAlGe  
and CuMnAs

蕭予誠

Yu-Cheng Shaw

指導教授：郭光宇博士

Advisor: Guang-Yu Guo, Ph.D.

中華民國 112 年 2 月

Feb, 2023





## 誌謝

謝謝我的指導教授郭光宇教授在我大四當專題生時就給我提點，也在研究上給我很高的自由度，可以去嘗試自己感興趣的主題。謝謝晏雲、明窩、威果，從我剛進研究室開始便給予我許多物理知識和研究觀念的刺激，成為我剛踏入研究領域的榜樣，謝謝昆翰和我一起聊天、討論研究遇到的疑惑和修改程式的技巧，給予我許多支持和鼓勵，謝謝 Babu Prasad 帶來不同的文化背景和觀點使得研究室的生活更豐富；謝謝晏雲、宗琦、勳奇、崇宇學長們讓我開拓研究視野並且幫助我追尋出國唸博士班的夢想，謝謝實驗室兩位單傳的學弟奕軒、雲辰，能夠問出不錯的問題和我討論，也一起負擔研究室的雜事，謝謝行政助理鳳霞，會替學生著想也會和我們聊天，謝謝我的家人、女友、高中和大學同學各自以他們的方式使我每天能充滿動力和活力。





## 摘要

由於實驗技術的進步、許多有前途的應用以及與拓撲的直接聯繫，非線性光學近年來受到廣泛關注。在非線性光學中，體光伏效應描述了二階電場下直流電的產生。拓撲半金屬被預測具有落在太赫茲範圍內的低頻發散。這可能開啟新的應用，例如光電探測和太赫茲通信。體光伏效應也被認為是一種有效的機制，可以在均質材料中利用太陽光發電。基於這種機制的太陽能電池與傳統 p-n 接面相比具有優勢，即產生的電壓不受帶隙值的限制。理論方面也很有趣：實驗和第一原理結果證實了貝里曲率與外爾半金屬中的量子化圓偏振注入電流之間的關係。由於圓偏振注入電流只是體光伏效應中四種電流之一，其餘電流是否存在其他關係成為一個自然的問題。最近的一篇論文確實進一步指出了與所有不同類型的體光伏電流相關的其他幾何量的存在。因此在本研究中，我們選擇了兩種材料，外爾半金屬 LaAlGe 和狄拉克半金屬 CuMnAs，它們擁有所有體光伏電流及其相應的幾何量，以實現對這些現象的真實材料研究。我們利用第一原理密度泛函理論得到的科恩-沈呂九軌道計算物理量和瓦尼爾插值方程。我也嘗試找出主要貢獻的區域和可能的機制。在 LaAlGe 中計算出接近 20 (毫安/伏特平方) 的大圓偏振注入電流和高達 0.5(毫安/伏特平方) 的線性偏移電流。當局部磁矩方向從 c 軸變為 b 軸時，CuMnAs 中的線性注入電流出現張量分量的變化和清晰的峰值。我在 LaAlGe、c 軸反鐵磁 CuMnAs 和 b 軸反鐵磁 CuMnAs 中系統性地研究了所有體光伏效應電導率和量子幾何量。此外，量子度規的布里淵區切片研究顯示了與輸出電流方向直接對應的有趣的不對稱行為。

關鍵字: 外爾半金屬, 狄拉克半金屬, 非線性光學, 體光伏效應,  
量子幾何量, 第一原理計算





# Abstract

Nonlinear optics (NLO) gains ample attention in recent years due to advances in experimental techniques, its many promising applications as well as its direct link to topology. Among NLO processes, bulk photovoltaic effect (BPVE) describes the generation of direct current (DC) under second-order electric field. In topological semimetals, it is predicted to have low-frequency divergence which falls within the terahertz regime. This could open new applications such as photodetection and terahertz communication. BPVE is also proposed to be an efficient mechanism to generate electricity from sunlight in a homogenous material. Solar cells based on this mechanism has the advantage over traditional p-n junction that the voltage generated is not limited by the value of bandgap. The theoretical aspect is also interesting: experimental and first principle results have confirmed the relation between Berry curvature and the quantized circular injection current in Weyl semimetals. Since the circular injection current is just one of the four currents in BPVE, it is natural to ask if there exist other relations for the remaining currents. A recent paper indeed further points out the existence of other geometric quantities related to all different kinds of BPVE current. In this study we thus choose two materials, Weyl semimetal LaAlGe and Dirac semimetal CuMnAs, that complete all the BPVE currents and their corresponding geometric quantities to realize a real material study of these phenomena. Kohn-Sham orbitals obtained by first-principle density functional theory are used to calculate physical quantities and Wannier interpolated function. I also try to find dominant regions and



possible mechanisms for various quantities. A large circular injection current close to  $20$  ( $\text{mA/V}^2$ ) and linear shift current up to  $0.5$  ( $\text{mA/V}^2$ ) is calculated in LaAlGe. Component change and a clear peak emerge for the linear injection current in CuMnAs when the local magnetic moment direction is changed from c-axis to b-axis. All the BPVE conductivities and quantum geometric quantities are systematically studied in LaAlGe, c-axis AFM CuMnAs, and b-axis AFM CuMnAs. Furthermore, the k-slice study of the quantum metric shows interesting asymmetry behavior directly corresponding to the outgoing current direction.

**Keywords :** Weyl semimetal, Dirac semimetal, nonlinear optics, bulk photovoltaic effect, quantum geometry, first-principle calculation

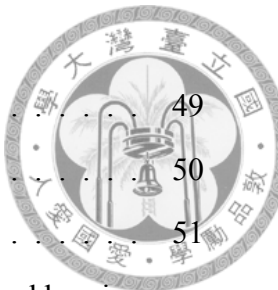


# Contents

誌謝	iii
摘要	v
<b>Abstract</b>	<b>vii</b>
<b>1 Introduction</b>	<b>1</b>
1.1 Nonlinear optical effects and bulk photovoltaic effect . . . . .	1
1.2 Topological semimetals . . . . .	3
1.2.1 Weyl semimetals: origin . . . . .	3
1.2.2 Topological aspects of Weyl semimetals . . . . .	4
1.2.3 Dirac semimetals . . . . .	6
<b>2 Theoretical background</b>	<b>9</b>
2.1 Nonlinear optics . . . . .	9
2.1.1 Independent particle approximation . . . . .	9
2.1.2 Length gauge derivation . . . . .	11
2.1.3 Interband and intraband transition . . . . .	16
2.1.4 Intraband transition and momentum conservation . . . . .	16
2.1.5 Quasi-particle lifetime and spontaneous emission . . . . .	17
2.1.6 Symmetry of conductivity tensors and quantum geometric quantities	17
2.2 Bulk photovoltaic effect in Dirac and Weyl Semimetals . . . . .	18
2.3 Quantum geometry in bulk photovoltaic effect . . . . .	21
2.4 Band structure and density functional theory . . . . .	23



2.4.1	Bloch theorem, Brillouin zone, and electronic band structure . . . . .	23
2.4.2	Hohenberg-Kohn theorem, Kohn-Sham equation, and exchange-correlation energy . . . . .	26
2.5	Computational methods . . . . .	27
2.5.1	Electronic structure . . . . .	27
2.5.2	Optical conductivity . . . . .	28
2.5.3	Matrix elements used in post-Wannier calculation . . . . .	28
2.5.4	Formulae used in post-Wannier calculations . . . . .	29
<b>3</b>	<b>Overview of physical properties of studied materials LaAlGe and CuMnAs</b>	<b>31</b>
3.1	LaAlGe . . . . .	31
3.1.1	Introduction and current state in research . . . . .	31
3.1.2	Structure, symmetry, and Brillouin zone of LaAlGe . . . . .	31
3.2	CuMnAs . . . . .	33
3.2.1	Introduction and current state in research . . . . .	33
3.2.2	Structure, symmetry, and Brillouin zone of CuMnAs . . . . .	33
<b>4</b>	<b>Bulk photovoltaic effect of nonmagnetic Weyl semimetal LaAlGe</b>	<b>35</b>
4.1	Electronic structure of LaAlGe . . . . .	35
4.2	Weyl point structure of LaAlGe . . . . .	36
4.3	Joint density of states and linear optical conductivity . . . . .	39
4.4	Shift and injection current conductivity spectrum . . . . .	41
4.5	<i>k</i> -path and <i>k</i> -slice analysis of conductivity and geometric quantities . . . . .	44
4.5.1	<i>k</i> -slice analysis validity check: Berry curvature . . . . .	45
4.5.2	<i>k</i> -slice analysis of circular injection conductivity and Berry curvature . . . . .	46
4.5.3	<i>k</i> -path analysis of linear shift conductivity and symplectic Christoffel symbol . . . . .	48
<b>5</b>	<b>Bulk photovoltaic effect of PT-symmetric antiferromagnetic Dirac semimetal CuMnAs</b>	<b>49</b>



5.1	Electronic structure of c-axis and b-axis AFM CuMnAs . . . . .	49
5.1.1	Projected band structure of c-axis AFM CuMnAs . . . . .	50
5.1.2	Density of states of c-axis AFM CuMnAs . . . . .	51
5.2	Joint density of states and linear optical conductivity of c-axis and b-axis AFM CuMnAs . . . . .	52
5.3	Shift and injection current conductivity spectrum for c-axis and b-axis AFM CuMnAs . . . . .	53
5.4	$k$ -path analysis of circular shift current and Christoffel symbol of the first kind of c-axis and b-axis AFM CuMnAs . . . . .	56
5.5	$k$ -slice analysis of linear injection conductivity and quantum metric of c- axis and b-axis AFM CuMnAs . . . . .	58
<b>6</b>	<b>Conclusion</b>	<b>61</b>
	<b>Bibliography</b>	<b>63</b>



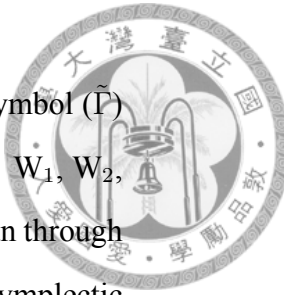


# List of Figures

1.1	Cartoon picture of bulk photovoltaic effect [3]. (a) Electron-hole pair produced by incoming photons. (b) Charge separation in the traditional p-n junction. (c) Charge separation in bulk photovoltaic effect. . . . .	2
1.2	Schematic band structure near (a) Weyl point and (b) Dirac point. . . . .	4
2.1	Band splitting of nearly free electrons [21]. (a) Band structure of the empty lattice. (b) Band structure of nearly free electrons. . . . .	25
3.1	Conventional unit cell for body-centered tetragonal LaAlGe (left), top view of the structure with $S_{4z}$ screw rotation axis and the Brillouin zone (bottom right). . . . .	32
3.2	Conventional unit cell for c-axis AFM CuMnAs (top left), b-axis view to demonstrate the $S_{2z}$ symmetry (bottom left) and the Brillouin zone (right). . . . .	34
3.3	Conventional unit cell for b-axis AFM CuMnAs (left), b-axis view to demonstrate the breaking of $S_{2z}$ symmetry (right). . . . .	34
4.1	DFT and Wannier band of nonmagnetic bulk LaAlGe. The Fermi level is shifted to 0 eV. . . . .	36
4.2	Weyl points in the $k_z=0$ plane of Brillouin zone. It can be seen from the schematic diagram below that this plot contains $W_1$ and $W_3$ that fall around 60 and 110 meV above the Fermi level respectively. . . . .	37
4.3	Dispersion relation near $W_1$ . The x-axis label is the same for the following two graphs. . . . .	38



4.4	Dispersion relation near $W_2$ . The x-axis label is the same as that of $W_1$ graphs. . . . .	38
4.5	Dispersion relation near $W_3$ . The x-axis label is the same as that of $W_1$ graphs. . . . .	39
4.6	Schematic diagram of $W_1$ , $W_2$ , $W_3$ , and their dispersion relation and location inside Brillouin zone. . . . .	39
4.7	Joint density of states and first-order optical conductivity of LaAlGe. . . . .	40
4.8	Independent component of circular injection current in LaAlGe with chemical potential equal to (a) $E_F$ , (b) shifted to $E_{W_1}$ , (c) $E_{W_2}$ and (d) $E_{W_3}$ . . . . .	42
4.9	Independent component of linear shift current in LaAlGe with chemical potential equal to (a) $E_F$ , (b) shifted to $E_{W_1}$ , (c) $E_{W_2}$ and (d) $E_{W_3}$ . . . . .	43
4.10	Berry curvature $k$ -slice of LaAlGe on X-Y plane containing $\Gamma$ point. Upper left: color map No.1, my code; Upper right: color map No.1, Wannier built-in function; bottom left: color map No.2, my code; bottom right: color map No.2, Wannier built-in function. . . . .	45
4.11	Berry curvature $k$ -slice of LaAlGe on X-Y plane containing $\Gamma$ point. Left: my code; right: Wannier built-in function with extreme value point taken out. . . . .	46
4.12	Circular injection conductivity and Berry curvature $k$ -slice of LaAlGe on X-Y plane containing $\Gamma$ point. Upper left: circular injection conductivity $\sigma_{xxz} \approx \sigma_{yyz}$ ; Upper right: Weyl point structure; bottom left: Berry curvature $\Omega_{yz}$ ; bottom right: circular injection conductivity spectrum with the selected peak pointed out. . . . .	47



4.13 <i>k</i> -path of linear shift conductivity and symplectic Christoffel symbol ( $\tilde{\Gamma}$ ) in LaAlGe. Each plot contains <i>k</i> -path across three Weyl points: $W_1$ , $W_2$ , and $W_3$ from left to right. Within each Weyl point, the <i>k</i> -path run through it in $k_x$ , $k_y$ , and $k_z$ from left to right. Upper panel: addition of symplectic Christoffel symbol with $\text{fac} = \pi e^3 / 2\hbar^2$ , the three colors represent setting $\mu = E_f$ , $E_{W_1}$ , and $E_{W_2}$ respectively. Lower panel: linear shift current, the three colors represent choosing the lowest peak frequency in $\mu = E_f$ , $E_{W_1}$ , and $E_{W_2}$ . . . . .	48
5.1 Upper left: band structure of c-axis and AFM CuMnAs. Upper right: band structure of b-axis and AFM CuMnAs. Lower left: partial density of states of c-axis and AFM CuMnAs. Lower right: Mn d-orbital projected band structure of c-axis AFM CuMnAs. . . . .	50
5.2 Left: Wannier and DFT band up to the full gap. Right: zoom in view of the b-axis CuMnAs band, it is gapped for all three energetically close points. . . . .	51
5.3 Joint density of states and first-order optical conductivity of c-axis AFM CuMnAs. . . . .	52
5.4 Joint density of states and first-order optical conductivity of b-axis AFM CuMnAs. . . . .	53
5.5 Independent component of linear injection and circular shift current in c-axis and b-axis AFM CuMnAs. (a) circular shift current of c-axis AFM CuMnAs, (b) circular shift current of b-axis AFM CuMnAs, (c) linear injection current of c-axis AFM CuMnAs, (d) linear injection current of b-axis AFM CuMnAs. . . . .	55
5.6 <i>k</i> -path of circular shift conductivity and Christoffel symbol of the first kind ( $\Gamma$ ) in b-axis CuMnAs. The <i>k</i> -path is the same high symmetry path used for drawing band structure, and $\Delta E_{min}$ is the <i>k</i> -point where the two gapped-out Dirac bands have the smallest energy difference. (a) Difference of Christoffel symbols of the first kind with $\text{fac} = \pi e^3 / 2\hbar^2$ . (b) Circular shift current with peak energy 0.01 eV. and (c) 0.03eV. . . . .	56



5.7	<i>k</i> -path of circular shift conductivity and Christoffel symbol of the first kind ( $\Gamma$ ) in c-axis CuMnAs. The $k$ -path is the same high symmetry path used for drawing band structure, $\Delta E_{min}$ is the $k$ -point where the two gapped-out Dirac bands have the smallest energy difference, and DP is the Dirac point. (a) Difference of Christoffel symbols of the first kind with $fac = \pi e^3 / 2\hbar^2$ . (b) Circular shift current with peak energy 0.018 eV, (c) 0.038eV, and (d) 0.052 eV. . . . .	57
5.8	Quantum metric $k$ -slice on X-Z plane containing $\Gamma$ point and linear injection spectrum of c-axis AFM CuMnAs. Upper left: $g_{yz}$ ; Upper right: $g_{xy}$ , the grey contour is the Fermi surface; bottom left: $g_{xz}$ ; bottom right: linear injection spectrum. . . . .	59
5.9	Quantum metric and Fermi surface contour $k$ -slice on X-Z plane containing $\Gamma$ point. Left: c-axis AFM CuMnAs; right: b-axis AFM CuMnAs. . . . .	60



# List of Tables

2.1	Jahn symbol of bulk photovoltaic conductivity tensors. . . . .	17
2.2	Time-reversal symmetry and PT- symmetry of bulk photovoltaic effect and its corresponding quantum geometry. $\tilde{\Gamma}$ is the symplectic Christoffel symbol and $\Gamma$ is the Christoffel symbol of the first kind. . . . .	18





# Chapter 1

## Introduction

In this chapter, I will give a brief introduction to the physical phenomena and the type of materials we choose to study. This allows us to gain a better understanding of the big picture. I will then give a detailed discussion regarding the bulk photovoltaic effect in chapter 2.

### 1.1 Nonlinear optical effects and bulk photovoltaic effect

Consider an ordinary electric field value around  $10^3\text{-}10^4(\text{V/m})$ , the energy describing the electric dipole interaction  $e\vec{r} \cdot \vec{E}$  is of order  $10^{-5}$  if we apply typical unit cell with size  $\approx 10^{-9}\text{m}$ . This is certainly much smaller than the Fermi energy of a typical material that is about  $1\text{-}10(\text{eV})$ . We can hence treat the external electric field as a perturbation in most cases [1]. Macroscopically, we thus expand our current in increasing order of electric field and associate each order with a conductivity [2]

$$j^c = \sigma_{(1)}^{c;a} E_a + \sigma_{(2)}^{c;ab} E_a E_b + \sigma_{(3)}^{c;abc} E_a E_b E_c + \dots \quad (1.1)$$

The first term is Ohm's law while other terms are nonlinear terms. The second-order term will vanish if the material possesses inversion symmetry. Since  $\mathbf{j}$  and  $\mathbf{E}$  change sign after inversion while  $\sigma^{(2)}$  stays unchanged due to inversion symmetry,  $\sigma^{(2)} = -\sigma^{(2)}$  can only be true when the conductivity is zero. If we consider the second-order term with



frequency dependence explicitly written out, we have

$$j^c(\omega_\Sigma) = \sigma_{(2)}^{c;ab} E_a(\omega_a) E_b(\omega_b), \quad (1.2)$$

where  $\omega_\Sigma = \omega_a + \omega_b$  can be seen from Fourier component or energy conservation. For two incident photons with energy  $\omega_a$  and  $\omega_b$ , if the asymmetric potential of the material only serves as the background in which electrons and photons are affected and electrons return to their initial positions after absorption and emission of photons, the energy of the outgoing photon should be the sum of the incoming photons.

For the second-order conductivity, we focus on the generation of DC current ( $\omega_\Sigma = 0$ ) called the bulk photovoltaic effect. There are two terms that contribute to this DC conductivity for nonmetallic materials [1][2]

$$\sigma_{(2)}^{c;ab} = \sigma_{shift}^{c;ab} + \sigma_{injection}^{c;ab}. \quad (1.3)$$

The shift current originates from the position difference of initial and excited electrons that causes a shift of charges (namely, current). Injection current is caused by the velocity difference between initial and excited electrons. Within the lifetime of the excited electron, this velocity difference keeps producing a net current. In other words, injection current saturates due to the finite lifetime.

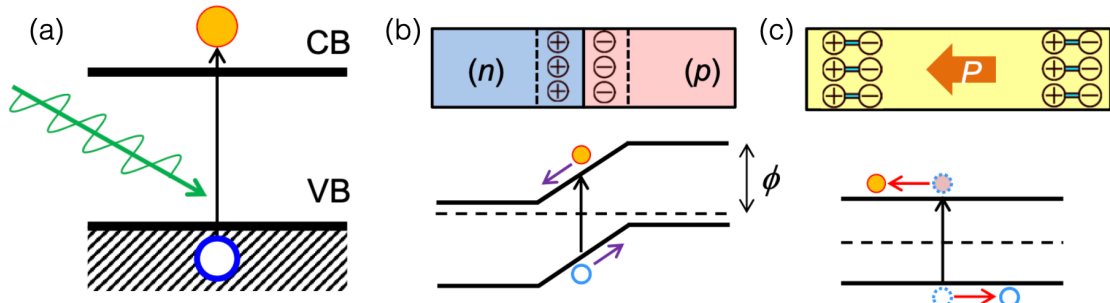


Figure 1.1: Cartoon picture of bulk photovoltaic effect [3]. (a) Electron-hole pair produced by incoming photons. (b) Charge separation in the traditional p-n junction. (c) Charge separation in bulk photovoltaic effect.

We can further separate the conductivities (both shift and injection) into two terms



regarding the polarization of the incident light [2].

$$\sigma^{c;ab} = \sigma_L^{c;ab} + i\sigma_C^{c;ab}.$$

It can be seen by writing out linearly and circularly polarized electric field for some particular frequency in its complex form,  $\vec{E}(t) = |E| e^{-i\omega t}(\cos\phi, \sin\phi, 0)$  and  $\vec{E}(t) = |E| e^{-i\omega t}(1, i, 0)$  respectively. Since the observable current is real, after we plug in these two electric fields into the second-order equation, we discovered only  $\sigma_L^{c;ab}$  can affect the current produced by linearly polarized light. Similarly,  $\sigma_C^{c;ab}$  will only affect the current produced by circularly polarized light.

## 1.2 Topological semimetals

### 1.2.1 Weyl semimetals: origin

Physicists found a band structure in condensed matter physics that mimics the energy-momentum dispersion relation of a Weyl fermion in high-energy physics. Dirac equation in the Weyl representation took the following form [4] [5]

$$\begin{pmatrix} -m & i(\partial_0 + \vec{\sigma} \cdot \vec{\nabla}) \\ i(\partial_0 - \vec{\sigma} \cdot \vec{\nabla}) & -m \end{pmatrix} \begin{pmatrix} \psi_L \\ \psi_R \end{pmatrix} = 0. \quad (1.5)$$

If we look at the massless case in momentum space, there will be two independent differential equations. We apply  $i\partial_t\psi = H\psi$  and get [4]

$$\begin{aligned} (H_L + \vec{\sigma} \cdot \vec{p})\psi_L &= 0 \\ (H_R - \vec{\sigma} \cdot \vec{p})\psi_R &= 0. \end{aligned} \quad (1.6)$$

For massless particles with positive energy, the energy eigenvalue  $E = |\vec{p}|$ . So the left-handed spinor has negative helicity ( $\vec{S} \cdot \vec{p}/|\vec{p}|$ ) while the right-handed spinor has positive helicity. This massless fermion with plus or minus helicity (=chirality as well in massless case) is called Weyl fermion. Since Weyl fermions of both chiralities have Hamiltonian



$\propto \vec{\sigma} \cdot \vec{p}$ , physicists called  $H = \vec{d}(\vec{k}) \cdot \vec{\sigma}$  the Hamiltonian near a Weyl point (the crossing point) in condensed matter physics. For any low energy excitation (small  $|\vec{k}|$  expansion) of a two-level system, if the dispersion is still linear, one can always do such expansion with appropriate  $\vec{d}(\vec{k})$  that is linear in  $\vec{k}_i$  (this is called linear Weyl node). We thus say we found a Weyl point whenever we see a band structure of such kind in figure (a) [6]

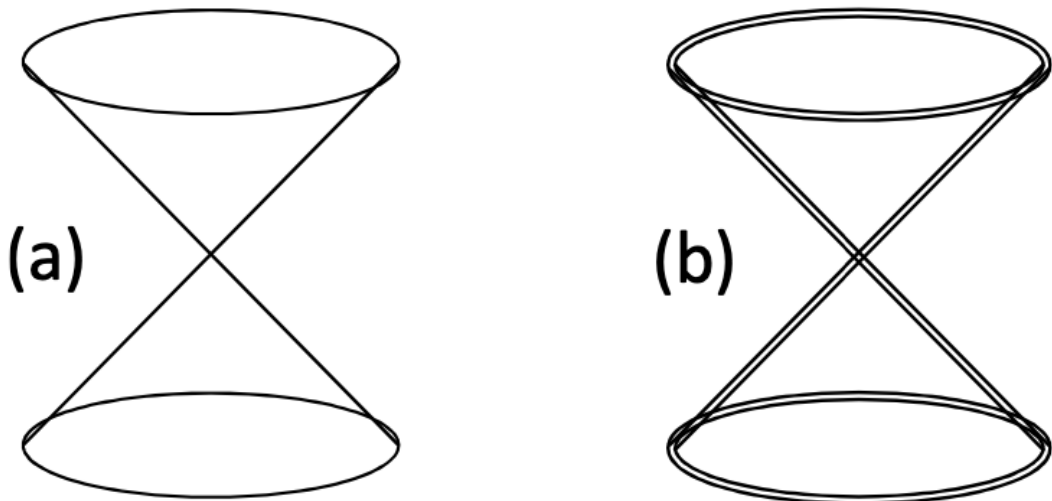


Figure 1.2: Schematic band structure near (a) Weyl point and (b) Dirac point.

The key features are linear dispersion and a 2-fold degenerate point. If the crossing happens near the Fermi level and the density of states is still low at the Fermi level, we call this type of material Weyl semimetals.

There are several differences between the high-energy and condensed matter Weyl points. In high-energy, the linear dispersion relation goes without the limit of  $|\vec{k}|$  being small and the chirality of Weyl fermions are fixed to  $\pm 1$ . Also, negative energy states with  $E = -|\vec{p}|$  may evoke positron in high energy physics yet they are completely normal electronic states in condensed matter physics. We hope to find the counterpart of chirality in condensed matter context. This is achieved by the topological charge (i.e. Berry index).

### 1.2.2 Topological aspects of Weyl semimetals

A famous geometrical phase in quantum mechanics called Berry phase [7] is the surface integral of Berry curvature or line integral of Berry connection defined respectively below



[6][8]

$$\mathbf{A}_n(\mathbf{k}) = -i \langle u_n(\mathbf{k}) | \nabla_{\mathbf{k}} | u_n(\mathbf{k}) \rangle$$

$$F_{n,ab}(\mathbf{k}) = \frac{\partial}{\partial k^a} A_{n,b}(\mathbf{k}) - \frac{\partial}{\partial k^b} A_{n,a}(\mathbf{k}),$$

or  $\mathbf{F}_n(\mathbf{k}) = \nabla_{\mathbf{k}} \times \mathbf{A}_n(\mathbf{k})$ .

For the Hamiltonian near Weyl point  $H = \mathbf{d}(\mathbf{k}) \cdot \sigma$ , we can compute its Berry curvature from the above definition and get [6]

$$\mathbf{F} = \frac{1}{2} \frac{\mathbf{d}}{d^3}. \quad (1.8)$$

Consider the map  $S_{\mathbf{k}}^2 \rightarrow S_{\mathbf{d}}^2$ , the infinitesimal surface normal vector of d-surface is the cross product of two infinitesimal change

$$d^2 \vec{a} = \frac{\partial \mathbf{d}}{\partial k_i} \times \frac{\partial \mathbf{d}}{\partial k_j} (dk_i dk_j), \quad (1.9)$$

where  $k_i$  and  $k_j$  are coordinates on the  $S_k^2$  as we learned in vector calculus.

Combining these facts, we found that the topological charge of such Hamiltonian is

$$Q_T \equiv \frac{1}{2\pi} \int_{S_k^2} d^2 \mathbf{a} \cdot \mathbf{F} = \frac{1}{2\pi} \int_{S_k^2} \frac{1}{2d^3} \mathbf{d} \cdot \left( \frac{\partial \mathbf{d}}{\partial k_i} \times \frac{\partial \mathbf{d}}{\partial k_j} \right) (dk_i dk_j). \quad (1.10)$$

The integral is exactly half the solid angle of the map  $S_{\mathbf{k}}^2 \rightarrow S_{\mathbf{d}}^2$  [6]. This justifies the topological aspect of this charge since the charge doesn't depend on the detailed geometry of the map  $S_{\mathbf{k}}^2 \rightarrow S_{\mathbf{d}}^2$  (i.e. band structure) but only depends on its topology.

Take  $H = \pm \mathbf{k} \cdot \sigma$  for example, the topological charge is  $\pm 1$  for each sign. This is called the chirality of Weyl nodes. Weyl nodes with positive chirality are the source of Berry curvature and Weyl nodes with negative chirality are the sink of Berry curvature.

Weyl nodes play an important role in several physical phenomena including the quantum Hall effect, anomalous Hall effect, and circular photovoltaic effect [8]. In the quantum Hall effect, the Hall conductance is proportional to the topological charge and is thus quantized. In the anomalous Hall effect, the magnitude of Hall conductance is determined by the k-space separation of Weyl nodes of opposite chirality. In the circular photogal-



vanic effect, the circular injection current is again proportional to the topological charge and quantized [9]. It can also be shown via edge modes of the stacking Chern insulator that, Weyl nodes of opposite chirality lead to the emergence of Fermi arcs in the surface Brillouin zone.

### 1.2.3 Dirac semimetals

The origin of Dirac semimetals is similar to that of Weyl semimetals. The main difference is we no longer have two  $2 \times 2$  blocks that are decoupled for Dirac fermions. The result is a 4-fold degenerate Dirac point and a 2-fold degeneracy in the linear dispersion region (see (b) of figure 1.2). We should also note that, unlike Weyl points that have nonzero topological charges, Dirac points have zero net Chern number since they could be viewed as a merger of two Weyl points having opposite charges. This will make Dirac points to be topologically unprotected and require space group symmetries to protect the Dirac points from being gapped.

Fu, Kane, and Mele proposed a simple model which successfully describes such a Dirac band structure. This model can be used to describe diamond lattice with spin-orbit coupling [4].

$$\mathcal{H} = t \sum_{\langle i,j \rangle, s} c_{i,s}^\dagger c_{j,s} + i \frac{\lambda_{so}}{a^2} \sum_{\ll i,j \gg, s, s'} c_{i,s}^\dagger (\hat{\sigma} \cdot \mathbf{d}_{ij}^{(1)} \times \mathbf{d}_{ij}^{(2)}) c_{j,s}. \quad (1.11)$$

In this model, the symmetry protecting the Dirac point is the cubic symmetry (can be seen from the isotropic  $t$ ).

In the symmetry aspect, Weyl points cannot exist in 3-dimension when both inversion ( $P$ ) and time-reversal ( $T$ ) symmetry are presented or when the combined  $PT$ -symmetry exists. This is because we want a nondegenerate band with degeneracy happening only at the Weyl point. Since  $(PT)^2 = -1$ , there will be 2-fold degeneracies if the system is invariant under  $PT$  (i.e.  $[H, PT] = 0$ ). That is not the case for Dirac semimetals. Though we need inversion symmetry to be broken to have second-order effects, systems that are odd in  $T$  yet possess a combined  $PT$ -symmetry can still be Dirac semimetals.

This provides a good platform for us to study the  $T$ -broken part of table 2.2.







# Chapter 2

## Theoretical background

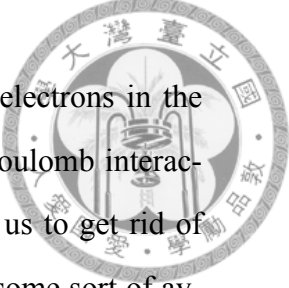
In this chapter, a more detailed theoretical understanding and interpretation of the bulk photovoltaic effect will be given first. Followed by the link between BPVE and quantum geometry as well as other analysis methods. The theoretical background of density functional theory from which we calculate the ground state Kohn-Sham orbitals will be introduced in the last part of this chapter.

### 2.1 Nonlinear optics

Derivation of bulk photovoltaic effect (BPVE) formulae can be obtained most generally by first considering a second-order conductivity with arbitrary frequencies  $\sigma^{(2)}(-\omega_\gamma; \omega_\alpha, \omega_\beta)$  where  $\omega_\gamma = \omega_\alpha + \omega_\beta$  and restrict the frequency sum to be zero:  $\omega_\alpha = -\omega_\beta = \omega$ . There are two other ways that can obtain the same result for BPVE, and they utilize Fermi's golden rule and Floquet formalism respectively. I will mainly focus on the length gauge derivation for general frequency due to its clarity and generality. Fermi's golden rule method will be briefly introduced later on for analysis purposes. After the formulae are derived, interpretation and theoretical analysis will be given.

#### 2.1.1 Independent particle approximation

Since the following derivations and calculations are all based on the independent particle approximation [1], I will introduce the approximation first. Independent particle



approximation means there is no explicit Coulomb repulsion between electrons in the Hamiltonian. However, this doesn't mean we completely neglect the Coulomb interaction between electrons, it is just simplified. This simplification allows us to get rid of the two-body electron-electron Coulomb interaction and replace it with some sort of averaged one-electron effective potential [10]. This greatly reduces the analysis and computational effort and can be justified by Fermi-liquid theory [10]. One possible scheme of such approximation is the Hartree approximation, if we further take into account the anti-symmetry requirement of the fermionic wave function, we can use the Hartree-Fock approximation or density functional theory.

The original Hamiltonian has the following form

$$\hat{H} = \hat{T} + \hat{V}_{ext} + \hat{U} = \sum_i^N \left( -\frac{\hbar^2 \nabla_i^2}{2m} + v_{ext}(\vec{r}_i) \right) + \frac{1}{2} \sum_{i \neq j}^N u(\vec{r}_i, \vec{r}_j), \quad (2.1)$$

where  $v_{ext}(\vec{r}_i)$  is the potential produced by nuclei and felt by electrons, and  $u(\vec{r}_i, \vec{r}_j)$  will be the electron-electron Coulomb repulsion. The approximation aims to write the Hamiltonian in the following form

$$H_0 = \sum_{i=1}^N \left( -\frac{\hbar^2 \nabla_i^2}{2m} + v_{eff}(\vec{r}_i) \right). \quad (2.2)$$

This  $H_0$  will serve as the ground state Hamiltonian describing the material of interest before being perturbed by incident light.

For Hartree approximation, the effective potential takes the form [10]

$$v_{eff}(\vec{r}) = \sum_{\mathbf{R}} \frac{-Ze^2}{|\vec{r} - \mathbf{R}|} + e^2 \int d\vec{r}' \frac{n(\vec{r}')}{|\vec{r} - \vec{r}'|}. \quad (2.3)$$

As for density functional theory used in this thesis, the effective potential contains an additional term other than the external ( $v_{ext}$ ) and Hartree ( $v_H$ ) potential

$$v_{xc}(\vec{r}) = \frac{\delta E_{xc}[n]}{\delta n(\vec{r})}. \quad (2.4)$$



This is the exchange-correlation potential that will be introduced in the last part of this chapter when I introduce the density functional theory framework.

The above approximation not only possesses advantages in the process of obtaining ground states, but it also allows us to describe the many-body system (our material) using scaled one-electron density matrix, at least for the expectation value of one-particle operators [1]. This means we need only to consider  $\{|u_{n,k}\rangle\}$  of the Bloch wave function as the basis for the matrix element, and there is no need to put two-or-more electron wave function into our set of basis. A more physical explanation is: we can now view the photo-absorption and the follow-up transition of electrons as a one-electron problem albeit a material is clearly composed of many electrons.

### 2.1.2 Length gauge derivation

To use length gauge with  $-e\vec{r} \cdot \vec{E}$  in the perturbed Hamiltonian, one needs to know how to express it in crystal momentum representation (CMR) [11]. The position operator in CMR can be split into two parts  $\mathbf{r} = \mathbf{r}_i + \mathbf{r}_e$  with one containing the highly divergent term and the other well-behaved [1]

$$\begin{aligned}\langle n\mathbf{k} | \mathbf{r}_i | m\mathbf{k}' \rangle &= \delta_{nm}[\delta(\mathbf{k} - \mathbf{k}')\xi_{nn} + i\nabla_{\mathbf{k}}\delta(\mathbf{k} - \mathbf{k}')] \\ \langle n\mathbf{k} | \mathbf{r}_e | m\mathbf{k}' \rangle &= (1 - \delta_{nm})\delta(\mathbf{k} - \mathbf{k}')\xi_{nm}.\end{aligned}\tag{2.5}$$

In the above expression,  $\xi_{nm}$  is defined as

$$\xi_{nm} = \frac{(2\pi)^3 i}{\Omega} \int_{\Omega} d^3\mathbf{r} u_{n\mathbf{k}}^*(\mathbf{r}) \nabla_{\mathbf{k}} u_{m\mathbf{k}}(\mathbf{r}),\tag{2.6}$$

where  $\Omega$  is the unit cell volume. Note that  $\xi_{nn}$  is gauge dependent with a nontrivial transformation

$$\xi'_{nn} = \xi_{nn} + \frac{\partial \varphi_n}{\partial k}\tag{2.7}$$

with respect to the  $U(1)$  gauge  $\exp[i\varphi_n(k)]$ , and the second term in  $\mathbf{r}_i$  is highly singular. We don't have to worry about these two facts because  $\mathbf{r}_i$  always appear in  $[\mathbf{r}_i, S]$  with a



simple operator  $S$  in our derivation, and the following identity holds [1]

$$\langle n\mathbf{k}| [\mathbf{r}_i, S] |m\mathbf{k}' \rangle = i\delta(\mathbf{k} - \mathbf{k}')(S_{nm})_{;\mathbf{k}}. \quad (2.8)$$

The generalized derivative is defined as

$$(S_{nm})_{;\mathbf{k}} \equiv \frac{\partial S_{nm}}{\partial \mathbf{k}} - iS_{nm}(\xi_{nn} - \xi_{mm}). \quad (2.9)$$

There are two important things to note. First, both  $\partial S_{nm}/\partial \mathbf{k}$  and  $\xi_{nn}$  are gauge-dependent yet they combined to form a gauge-independent quantity  $(S_{nm})_{;\mathbf{k}}$ . Second, this generalized derivative plays a similar role as the covariant derivative in differential geometry, and this is the first glimpse of the connection between general NLO and (quantum) geometry that would be revealed partially in this thesis.

After the CMR of the position operator is taken into account, we use [1]

$$\mathbf{J} = \overline{Tr}(\mathbf{j}_\mu \rho) \quad (2.10)$$

to link the microscopic description (velocity operator inside  $\mathbf{j}_\mu$  and density matrix) and macroscopic quantity (current). The overline on trace indicates spatial average and

$$\mathbf{j}_\mu = \frac{e}{2}(\mathbf{v}\mu + \mu\mathbf{v}), \quad \mu \equiv |\mathbf{r}><\mathbf{r}|. \quad (2.11)$$

We have  $d\mathbf{P}/dt = \mathbf{J}$  for macroscopoic polarization density  $\mathbf{P}$  and current density  $\mathbf{J}$ . In other words, to get macroscopic current we need to take two averages: the state average represented by density operator  $\hat{\rho} = \sum_i p_i |\psi_i\rangle \langle \psi_i|$  and spatial average represented by the bar over trace  $\overline{Tr}$ . By the cyclic invariance of trace and under the long-wavelength limit, the current density takes the form

$$\mathbf{J}^a = \frac{e}{m} \sum_{nm\mathbf{k}} p_{mn}^a \rho_{nm}, \quad (2.12)$$

where  $p_{mn}^a$  is the momentum matrix element.



Next, we need to find an expression for the density matrix in increasing order of the perturbed electric field  $E^a$ , insert it back into the above equation, and get the response current for each order. To do so, we rely on the dynamical equation for the density operator in Schrödinger picture

$$i\hbar \frac{d\rho}{dt} = [H, \rho], \quad (2.13)$$

and transform the whole equation to interaction picture by  $\theta \rightarrow \tilde{\theta}(t) = e^{iH_0 t/\hbar} \theta e^{-iH_0 t/\hbar}$ .

This gives

$$i\hbar \frac{d\tilde{\rho}}{dt} = [H_{int}, \tilde{\rho}], \quad (2.14)$$

where  $H_{int}$  is the interacting Hamiltonian which in our case is  $-e\tilde{\mathbf{r}} \cdot \mathbf{E}$ . We solve it by direct integration [1].

$$i\hbar \tilde{\rho}(t) = i\hbar \rho_0 + \int_{-\infty}^t [-e\tilde{\mathbf{r}}(t') \cdot \mathbf{E}(t'), \tilde{\rho}(t')] dt'. \quad (2.15)$$

If we label  $\rho^{(N)}$  as the density containing the electric field in  $N$ -th order, we have the iterative relation [1]

$$i\hbar \tilde{\rho}_{nm}^{(N+1)}(t) = \frac{ie}{\hbar} \int_{-\infty}^t dt' e^{i\omega_{nm} t'} \mathbf{E}(t') \cdot [\mathbf{R}_e + \mathbf{R}_i], \quad (2.16)$$

where

$$\begin{aligned} \mathbf{R}_e &= \sum_l \left[ \mathbf{r}_{nl} \rho_{lm}^{(N)} - \rho_{nl}^{(N)} \mathbf{r}_{lm} \right] \\ \mathbf{R}_i &= i \left[ \rho_{nm}^{(N)} \right]_{,\mathbf{k}}. \end{aligned} \quad (2.17)$$

The unperturbed density is the Fermi-Dirac distribution  $\rho_{nm}^{(0)} = \delta_{nm} f(\hbar\omega_n)$ . This completes the route to obtain  $N$ -th order result with respect to the electric field.

Note in evaluating the indefinite integral after we put  $\mathbf{E}(t) = \mathbf{E} e^{i\omega t}$  into the integrand above,

$$\int_{-\infty}^t dt' e^{iw_{nm} t'} e^{-i\omega t'} \quad (2.18)$$

will appear for first order  $\tilde{\rho}_{nm}^{(1)}(t)$ . We have to include the lifetime of the electrons and add a small  $i\epsilon$  in the  $\omega_{nm}$  in the exponential. After this, the integral is straightforward.



We show here the first and second-order results in terms of susceptibility  $\chi$  [1]. One can easily change between conductivity and susceptibility by noting  $J = \sigma E = dR/dt$  and  $P = \chi E$  which gives  $i\omega\chi = \sigma$ . This is also true in the second-order with  $\omega$  replaced by the sum of the two incident frequency  $\omega \rightarrow \omega_\Sigma$ .

$$\chi_{ba}^{(1)}(-\omega; \omega) = \frac{e^2}{\hbar} \sum_{nmk} \frac{r_{mn}^b r_{nm}^a f_{mn}}{\omega_{nm} - \omega} \quad (2.19)$$

with the first Cartesian index representing the outgoing current direction and the second index representing the incoming electric field direction. For the second-order susceptibility, we write it as  $\chi^{(2)} = \chi_\chi^{(2)} + \chi_\sigma^{(2)}$  where  $\chi_\chi^{(2)}$  is defined by putting the second-order density into  $P_\chi \equiv e\overline{Tr}(\mathbf{r}_e\rho)$  [1].

$$\begin{aligned} \chi_{\chi cba}^{(2)}(-\omega_\Sigma; \omega_\beta, \omega_\alpha) &= \frac{2e^3}{\hbar^2} \sum_{nmlk} \frac{r_{mn}^c}{\omega_{nm} - \omega_\Sigma} \left( \frac{r_{nl}^b r_{lm}^a f_{ml}}{\omega_{lm} - \omega_\alpha} - \frac{r_{lm}^b r_{nl}^a f_{ln}}{\omega_{nl} - \omega_\alpha} \right) \\ &\quad + \frac{2ie^3}{\hbar^2} \sum_{nmk} \frac{r_{mn}^c}{\omega_{nm} - \omega_\Sigma} \left( \frac{r_{nm}^a f_{mn}}{\omega_{nm} - \omega_\alpha} \right)_{;k^b}. \end{aligned} \quad (2.20)$$

For the first summation, the  $r_{mn}^c$  outside the parenthesis comes from the outgoing momentum  $p^c$  and the two terms inside the parenthesis come from the commutator of  $\mathbf{r}_e$  and first-order density  $\rho^{(1)}$ . For the second summation, the parenthesis is replaced by the generalized derivative of the first-order density. The  $\chi_\sigma^{(2)}$  term has contributions from both  $\rho^{(1)}$  and  $\rho^{(2)}$  [1]

$$\begin{aligned} \chi_{\sigma cba}^{(2)}(-\omega_\Sigma; \omega_\beta, \omega_\alpha) &= \frac{2e^3}{\hbar^2} \frac{1}{i\omega_\Sigma^2} \sum_{nmk} \Delta_{mn}^c r_{mn}^b \left( \frac{r_{nm}^a f_{mn}}{\omega_{nm} - \omega_\alpha} \right) \\ &\quad + \frac{2e^3}{\hbar^2} \frac{1}{i\omega_\Sigma} \sum_{nmk} (r_{mn}^b)_{;k^c} \left( \frac{r_{nm}^a f_{mn}}{\omega_{nm} - \omega_\alpha} \right). \end{aligned} \quad (2.21)$$

The first summation comes from the trace of  $\mathbf{p}_i \rho^{(2)}$  where  $\mathbf{p}_i$  is the intraband momentum operator. The second-order density will bring an extra  $1/\omega_\Sigma$  due to the existence of the intraband momentum operator, resulting in a total of  $i\omega_\Sigma^2$  in the denominator. The second summation is from the trace of  $[\mathbf{r}_i, -e\mathbf{r}_e \cdot \mathbf{E}] \rho^{(1)}$  so we see a single  $(r_{mn}^b)_{;k^c}$ . This term is also first calculated in  $\mathbf{J}$  so there is a single  $i\omega_\Sigma$  in the denominator. This is why we can



view the first term as current injection  $d\mathbf{J}/dt$  and the second term as current  $\mathbf{J}$ . These two terms are the leading diverging terms when we took the limit  $\omega_\Sigma \rightarrow 0$  for DC generation, and they give the injection current and shift current respectively. I gave the formulae here for the current injection [1]

$$\nu^{(2)}(0; \omega, -\omega) = -\frac{2\pi e^3}{\hbar^2} \sum_{nmk} \Delta_{mn}^c r_{mn}^b r_{nm}^a f_{mn} \delta(\omega_{nm} - \omega), \quad (2.22)$$

and the current term [1]

$$\sigma^{(2)}(0; \omega, -\omega) = -i \frac{\pi e^3}{\hbar^2} \sum_{nmk} \left[ (r_{mn}^b)_{;k^c} r_{nm}^a - r_{mn}^b (r_{nm}^a)_{;k^c} \right] f_{mn} \delta(\omega_{nm} - \omega). \quad (2.23)$$

Note both of the above expressions satisfy the intrinsic permutation symmetry

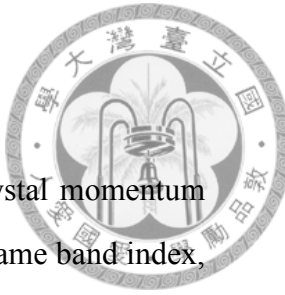
$$\sigma_{c;ba}^{(2)}(-\omega_\Sigma; \omega_\beta, \omega_\alpha) = \sigma_{c;ab}^{(2)}(-\omega_\Sigma; \omega_\alpha, \omega_\beta). \quad (2.24)$$

One can write the current injection in conductivity form and rewrite the shift current in terms of shift vector. This will give  $\sigma_{c;ab}^{(2)}(0; \omega, -\omega) = \sigma_{shift}^{c;ab} + \sigma_{inj}^{c;ab}$  and [2]

$$\begin{aligned} \sigma_{shift}^{c;ab} &= -\frac{\pi e^3}{\hbar^2} \int_{\mathbf{k}} \sum_{nm} (R_{mn}^{c,a} - R_{nm}^{c,b}) r_{nm}^b r_{mn}^a f_{nm} \delta(\omega_{mn} - \omega) \\ \sigma_{inj}^{c;ab} &= -\tau \frac{2\pi e^3}{\hbar^2} \int_{\mathbf{k}} \sum_{nm} \Delta_{mn}^c r_{nm}^b r_{mn}^a f_{nm} \delta(\omega_{mn} - \omega). \end{aligned} \quad (2.25)$$

For the above expression,  $\int_{\mathbf{k}} = \int d^d k / (2\pi)^d$ , shift vector  $R_{mn}^{c,a} = r_{mm}^c - r_{nn}^c + i\partial_c \log(r_{mn}^a)$ ,  $r_{nm}^a = \langle m | i\partial_a | n \rangle$  where  $\partial_a$  here indicates  $\partial/\partial_{k_a}$ ,  $f_{nm} = f_n - f_m$  is the difference of the two Fermi-Dirac distribution at band  $n$  and  $m$ ,  $\hbar\omega_{mn} = \hbar\omega_m - \hbar\omega_n$  is the energy difference and  $\Delta_{mn}^c = v_{mm}^c - v_{nn}^c$  with  $v_{mn}^c = \hbar^{-1} \langle m | \partial_c | n \rangle$ . Here,  $\{|n\rangle\}$  are the energy eigenstates  $H|n\rangle = \hbar\omega_n|n\rangle$ .

After formulae for second-order response and BPVE have been derived, I aim to comment on the meaning of interband and intraband transition, address momentum conservation issues and state how quasi-particle lifetime or spontaneous emission is taken into account. The link between NLO and linear optics will be given in section 2.5.2.



### 2.1.3 Interband and intraband transition

The concept of interband and intraband transitions comes from the crystal momentum representation of position operator  $\langle n|\mathbf{r}|m \rangle$ . When  $n$  and  $m$  are the same band index,  $[\mathbf{r}_i, \rho]$  will give rise to the generalized derivative. The  $\xi_{nn}$  in the generalized derivative can be linked to the Berry connection for band  $n$ , giving us a way to probe the geometrical phase. For interband transition,  $\mathbf{r}_{nm}$  simply gives the transition probability of electron jumping from band  $m$  to band  $n$  without information of geometric phases. As a result, terms in general NLO formulae can be endowed with a geometrical meaning much more easily if they contain intraband transitions. Some [12] also observed that in the second harmonic generation, intraband terms are more free-electron-like while interband terms are more atomic-like thus intraband contributions will be more dominant if you have a more dispersive band structure.

### 2.1.4 Intraband transition and momentum conservation

Often times we see pictures illustrating the intraband transition process having electrons going into a neighboring state with an infinitesimal momentum difference  $\Delta k$  within the same band. We know the momentum carried by photons should be approximately zero to that of electrons. So where did the electron gains finite momentum to produce the current? This is the question we're answering in this paragraph.

As mentioned previously, intraband terms can produce  $r_{nm}^a r_{mn}^c \Delta_{mn}^b$  in the case of injection current. To elaborate the detailed transition process, we can view  $r_{nm}^a r_{mn}^c$  as the transition amplitude (in the sense of Fermi's golden rule) from band  $n$  to  $m$  excited by electric field along  $a$  and  $c$  direction. This means the current is produced via: an electron being excited from band  $n$  to  $m$  and the velocity difference between those two bands causes the current.

In conclusion, intraband transition gives information about the velocity of electrons. Electrons gain momentum from being excited to another state that has a different velocity and not from the photon itself. This ensures the momentum conservation to still be valid. Also note that for second-order effect, terms originating from intraband transition can



still have interband information because now we have the inter-intraband contribution  $\rho^{ie} \sim [\mathbf{r}_i, [\mathbf{r}_e, \rho^{(0)}]]$ . This is why we can still talk about the velocity of different bands when we are talking about (partially) intraband contribution.

### 2.1.5 Quasi-particle lifetime and spontaneous emission

One question remains: does the formula include the consideration of quasi-particle lifetime or spontaneous emission? If so, where does it appear in our derived formulae?

Spontaneous emission says electrons will have a probability to drop back to their original state after it has been excited. The rate at which the excited state is decaying into the ground state can be described by Fermi's golden rule under time-dependent perturbation theory

$$\Gamma_{i \rightarrow f} = \frac{2\pi}{\hbar} |\langle f | H' | i \rangle|^2 \rho(E_f), \quad (2.26)$$

where  $\Gamma$  is the probability for  $i \rightarrow f$  transition per unit time. The question is: do we include both the  $i \in occ \rightarrow f \in unocc$  and the decay process or just one of them? We notice that other than the position (or velocity) difference and the one-way ( $i \in occ \rightarrow f \in unocc$ ) transition probability, there is a Fermi-Dirac difference. It serves as the net result of the two-way process mentioned above. So the quasi-particle or spontaneous emission process should already be taken into account.

### 2.1.6 Symmetry of conductivity tensors and quantum geometric quantities

I list here the symmetry properties of all four bulk photovoltaic effects [2]. Combined with the space group of studied materials, they can give non-zero tensor components of the conductivity tensors.

Tensor	$\sigma_{inj,L}^{c;ab}$	$\sigma_{inj,C}^{c;ab}$	$\sigma_{sh,L}^{c;ab}$	$\sigma_{sh,C}^{c;ab}$
Jahn symbol	$aV[V^2]$	$V\{V^2\}$	$V[V^2]$	$aV\{V^2\}$

Table 2.1: Jahn symbol of bulk photovoltaic conductivity tensors.



Notations of the Jahn symbol are:  $a$  indicates the tensor will change sign under time-reversal,  $[V^2]$  indicates the tensor is even under the exchange of the last two indices, and  $\{V^2\}$  indicates the tensor will change sign under the exchange of the last two indices.

I use the *FINDSYM* program [13][14] to reexamine the (magnetic) space group and symmetry operator of my materials. The resulting (magnetic) space group along with the symmetry properties listed above can be fed into Bilbao crystallographic server to get the non-zero tensor component for each BPVE tensor. I analyze only the non-zero components after the calculation.

Other symmetries that play major roles in BPVE and quantum geometry are the time-reversal symmetry and the parity-time (PT) symmetry. From [2], the important table is given

Response	Linear injection	Circular injection	Linear shift	circular shift
Parity under $T$	-	+	+	-
Parity under $PT$	+	-	-	+
Geometric quantities	Quantum metric	Berry curvature	$\tilde{\Gamma}$	$\Gamma$

Table 2.2: Time-reversal symmetry and PT-symmetry of bulk photovoltaic effect and its corresponding quantum geometry.  $\tilde{\Gamma}$  is the symplectic Christoffel symbol and  $\Gamma$  is the Christoffel symbol of the first kind.

All the geometric quantities mentioned here will be defined and explained in section 2.2 and 2.3 in this chapter.

## 2.2 Bulk photovoltaic effect in Dirac and Weyl Semimetals

From equation 2.25 we can calculate the shift and injection current for the following  $d_M \times d_M$  Hamiltonian [2]

$$H(\mathbf{k}) = -\mu(\mathbf{k}) + \sum_i f_i(\mathbf{k})\Gamma_i, \quad (2.27)$$



where  $\Gamma_i$  are mutually anticommuting matrices. For example,  $\Gamma_i$  are the three Pauli matrices for  $d_M = 2$  and five Dirac gamma matrices when  $d_M = 4$ . Notice this Hamiltonian will give us a single Weyl (Dirac) point in the two-band (four-band) case if we take  $f_i(\mathbf{k}) = k_i$ .

Starting with the injection current conductivity, we first use  $\Delta_{mn}^c = \partial_c \omega_{mn}$  so that  $\Delta_{mn}^c \delta(\omega_{mn} - \omega) = \partial_c \Theta(\omega_{mn} - \omega)$ . Then we use integral by part and generalized Stokes theorem to obtain the following form [2]

$$\sigma_{inj}^{c;ab} = -\tau \frac{2\pi e^3}{\hbar^2} \int_{\omega_{cv}=\omega} \frac{d^{d-1}k}{(2\pi)^d} (\hat{n} \cdot \hat{c}) Q_{ba}, \quad (2.28)$$

with

$$Q_{ba} = \sum_{n \in occ} \sum_{m \in unocc} r_{nm}^b r_{mn}^a. \quad (2.29)$$

This term is the quantum geometric tensor and its meaning will be clear later on. From here, we make use of the above Hamiltonian and get our answer in terms of  $f_i(\mathbf{k})$ . The quantum geometric tensor will become [2]

$$Q_{ba} = \frac{\hbar^2}{4f^2} \sum_{n \in occ} \sum_{m \in unocc} v_{nm}^b v_{mn}^a \quad (2.30)$$

because  $r_{nm}^a = v_{nm}^a / i\omega_{nm}$  and  $\hbar\omega_{unocc} - \hbar\omega_{occ} = 2\sqrt{\sum f_i^2} = 2f$ . The velocity matrix element now is

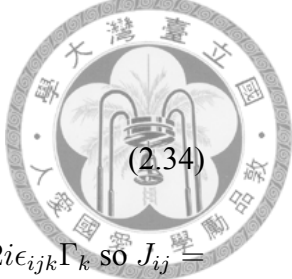
$$\hbar v_{nm}^b = \langle n | \partial_b H | m \rangle = \sum \partial_b f_i \langle n | \Gamma_i | m \rangle, \quad (2.31)$$

so by writing  $\Gamma_i \Gamma_j = \frac{1}{2} \{ \Gamma_i, \Gamma_j \} + \frac{1}{2} [\Gamma_i, \Gamma_j]$  and gamma matrices' commutation relations  $\{ \Gamma_i, \Gamma_i \} = 2\delta_{ij}$  we obtain [2]

$$Q_{ba} = \sum_{i,j} \partial_b f^i \partial_a f^j \frac{d_M (\delta_{ij} - \hat{f}_i \hat{f}_j + i J_{ij})}{8f^2}. \quad (2.32)$$

the first term in the parenthesis is from

$$\langle m | \Gamma_j | n \rangle = -\frac{f_j}{f} \delta_{nm} \equiv \hat{f}_j \delta_{nm} \quad (2.33)$$



for  $m, n \in occ$ , and

$$J_{ij} \equiv \frac{i}{d_M} \sum_{n \in occ} \langle n | [\Gamma_i, \Gamma_j] | n \rangle. \quad (2.34)$$

For two-band systems,  $\Gamma_i$  are just Pauli matrices and we have  $[\Gamma_i, \Gamma_i] = 2i\epsilon_{ijk}\Gamma_k$  so  $J_{ij} = -\epsilon_{ijk}\hat{f}_k$ .

Next, we turn to look at the shift current conductivity tensor. It can be written as [2]

$$\sigma_{shift}^{c;ab} = -i \frac{2\pi e^3}{\hbar^2} \int_{\mathbf{k}} C_{bca} f_{vc} \delta(\omega_{cv} - \omega), \quad (2.35)$$

where  $v$  and  $c$  stand for valence and conduction band and

$$C_{bca} = -i \sum_{n \in occ} \sum_{m \in unocc} R_{mn}^{c,a} r_{nm}^b r_{nm}^a \quad (2.36)$$

is the quantum geometric connection. Using similar relations shown above, we can also write it in terms of  $f_i(\mathbf{k})$  [2]

$$C_{bca} = \sum_{i,j} \frac{d_M(\delta_{ij} - \hat{f}_i \hat{f}_j + i J_{ij})}{8f^2} \times \left[ \partial_b f^i \partial_a \partial_c f^j - \frac{1}{f} (\partial_b f^i \partial_c f^j \partial_a f + \partial_b f^i \partial_a f^j \partial_c f) \right]. \quad (2.37)$$

If we focus on only two nondegenerate bands, the three bands' virtual transition

$$\sum_{\omega_p \neq \omega_m, \omega_n} \left( \frac{v_{mp}^c v_{pn}^a}{\omega_{mp}} - \frac{v_{mp}^a v_{pn}^c}{\omega_{pn}} \right) \quad (2.38)$$

will vanish and from equation 2.36 we will have [2]

$$C_{bca} = \sum_{n \in occ} \sum_{m \in unocc} r_{nm}^b r_{mn,c}^a. \quad (2.39)$$

Though both the shift and injection conductivity expression above is exact only for two or four bands, it still serves as a good approximation under some criteria [2]. In short, the conditions are fulfilled by focusing on the low energy regime of the spectrum where small  $\omega$  gives small  $(\omega/\Delta E)^2$  ( $\Delta E$  is the energy difference of crossing bands and the



other bands). So I choose equation 2.29 and equation 2.39 as the formulae to code into the PostWannier [15] framework.

## 2.3 Quantum geometry in bulk photovoltaic effect

After all the formulae regarding the model Hamiltonian 2.27 are derived, I would like to show their geometrical meaning. First, to see why equation 2.29 has geometric meaning, we choose a particular pair of occupied bands  $n_1$  and  $n_2$ , then [2]

$$\begin{aligned}
 Q_{ab} &= \sum_{m \in unocc} r_{n_1 m}^a r_{m n_2}^b \\
 &= \sum_{m \in unocc} \langle \partial_a n_1 | m \rangle \langle m | \partial_b n_2 \rangle \\
 &= \frac{1}{2} \left[ \langle \partial_a n_1 | \partial_b n_2 \rangle - \sum_{p \in occ} \langle \partial_a n_1 | p \rangle \langle p | \partial_b n_2 \rangle + (a \leftrightarrow b) \right] \\
 &\quad + \frac{1}{2} \left[ \langle \partial_a n_1 | \partial_b n_2 \rangle - \sum_{p \in occ} \langle \partial_a n_1 | p \rangle \langle p | \partial_b n_2 \rangle - (a \leftrightarrow b) \right] \\
 &\equiv (g_{ab})_{n_1 n_2} - \frac{i}{2} (F_{ab})_{n_1 n_2}.
 \end{aligned} \tag{2.40}$$

We can immediately recognize  $(F_{ab})_{n_1 n_2}$  as the non-Abelian berry curvature

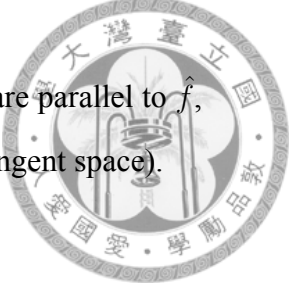
$$\mathbf{F}_{ab} = \partial_a \mathbf{A}_b - \partial_b \mathbf{A}_a - i [\mathbf{A}_a, \mathbf{A}_b], \tag{2.41}$$

while the real part should be interpreted as the quantum metric. This is because if we consider the map  $\mathbf{f} : \mathbf{BZ} \rightarrow \mathbb{R}^{d_\Gamma}$  from Brillouin zone to the  $\mathbf{f}$ -space, the quantum geometric tensor can be seen as a pullback from the tangent space of  $\mathbf{f}$ -space to that of the Brillouin zone [2].

$$g_{ab} = \sum_{i,j} \partial_a f_i \partial_b f_j \eta_{ij} = \sum_{i,j} \partial_a f_i \partial_b f_j \frac{d_M(\delta_{ij} - \hat{f}_i \hat{f}_j)}{8f^2}. \tag{2.42}$$

When we get rid of the transformation of tangent vectors  $\partial_a f_i$ , we see  $\eta_{ij}$  is the metric on tangent space of  $\mathbf{f}$  that form a generalized Bloch sphere ( $f = 1$ ).

$$ds^2 = \eta_{ij} df^i df^j. \tag{2.43}$$



It can be seen as follow:  $\delta_{ij} - \hat{f}_i \hat{f}_j$  projects out vector components that are parallel to  $\hat{f}$ , leaving only product of components that are perpendicular to  $\hat{f}$  (in the tangent space).

Similarly, from equation 2.37 we can give different parts of it geometrical meaning as the connection. First, we introduce the Christoffel symbol of the second kind as a quantity that tells us how to compare vectors lying in adjacent tangent spaces.

$$\partial_i \mathbf{e}_j = \sum_k \gamma_{ij}^k \mathbf{e}_k. \quad (2.44)$$

It can be expressed by the metric [16]

$$\gamma_{ij}^k \equiv \sum_l \eta^{kl} \frac{1}{2} (\partial_i \eta_{jl} + \partial_j \eta_{il} - \partial_l \eta_{ij}), \quad (2.45)$$

where we would take the metric to be that on the generalized Bloch sphere mentioned previously. Note we have to use the same coordinate system for all indices in the defining equation of the Christoffel symbol, so here  $\partial_i = \partial/\partial f_i$ . We can utilize the fact that  $\eta^{il} \eta_{jl} = \delta_j^i$ , calculate the metric inverse and its partial derivatives with respect to  $f_i$  and multiply by  $\eta$  to get the Christoffel symbol in terms of  $f_i$ . For example, the first term in equation 2.45 can be calculated by  $-\frac{1}{2}(\partial_i \eta^{kl})\eta_{jl}$ . The result in terms of  $f_i$  is [2]

$$\gamma_{ij}^k = -\frac{f_i}{f^2} (\delta_{jk} - \hat{f}_j \hat{f}_k) - \frac{f_j}{f^2} (\delta_{ik} - \hat{f}_i \hat{f}_k). \quad (2.46)$$

Now we lower the index to get the Christoffel symbol of the first kind, yet we combine another part contracted by symplectic form  $\epsilon_{kl}$  rather than the metric tensor  $\eta_{kl}$  [2].

$$\begin{aligned} c_{kij} &\equiv \gamma_{kij} - i\tilde{\gamma}_{kij} \\ &\equiv \sum_l \eta_{kl} \gamma_{ij}^l - i\epsilon_{kl} \gamma_{ij}^l. \end{aligned} \quad (2.47)$$

This gives us the geometric connection on the generalized Bloch sphere. Finally, we can



do the coordinate transformation specified by  $f_i(\mathbf{k})$  and get [2]

$$C_{cab} = \sum_{i,j,k} \partial_c f_k \partial_a f_i \partial_b f_j c_{kij} + \sum_{i,j} \partial_c f_i \partial_a \partial_b f_j q_{ij}. \quad (2.48)$$

This shows that the quantum geometric connection defined previously does indeed has the meaning of a connection.

## 2.4 Band structure and density functional theory

In the first part of this section, I aim to go through important concepts in solid-state physics for systems that possess periodicity. This includes the Bloch theorem, Brillouin zone, and electronic band structure. In the second part of this section, I will introduce the density functional theory framework we use to get our Kohn-Sham orbitals of materials. This contains the Hohenberg-Kohn theorem [17], Kohn-Sham equation [18], and exchange-correlation energy.

### 2.4.1 Bloch theorem, Brillouin zone, and electronic band structure

If the system of interests has a periodicity in real space, the energy eigenstates of the system have to obey Bloch theorem (1-D version)

$$\psi(x) = e^{ikx} u(x) \text{ and } u(x+a) = u(x), \quad (2.49)$$

where  $a$  is the real space periodicity.

We demonstrate here a group theory proof of the Bloch theorem [19]. First, notice all translation operators are Abelian ( $\hat{T}_1 \hat{T}_2 = \hat{T}_2 \hat{T}_1$ ) and unitary ( $\langle \hat{T}\psi_1 | \hat{T}\psi_2 \rangle = \langle \psi_1 | \psi_2 \rangle$ ). For one-dimensional space, the group of translational operators is cyclic since all elements can be generated by the smallest shift. Also, group theory tells us that all the irreducible representations of Abelian groups are one-dimensional [19]. Hence

$$\psi'(x) \equiv \hat{T}\psi(x) = \zeta\psi(x), \quad (2.50)$$



where  $\zeta$  is the one-dimensional irreducible representation. Since the wave functions are normalized,  $\zeta$  will have to satisfy  $|\zeta| = 1$ . This gives  $\zeta = e^{ika}$  for some  $k \in \mathbb{R}$ . We can further restrict  $k$  to be in  $-\frac{\pi}{a} \leq k \leq \frac{\pi}{a}$  since  $e^{i(ka+2\pi)} = e^{ika}$ . This is the simplest example of the (first) Brillouin zone. Finally, because  $\hat{T}^N = 1$ ,  $k$  can take only certain values  $k = (2\pi/Na)j$ . This completes the proof and it can be easily generalized to three-dimensional cases.

Bloch theorem implies we can always restrict the crystal momentum in a small part of the  $k$ -space called the first Brillouin zone. To see this, write the energy eigenstate labeled by crystal momentum in

$$\psi_{\vec{k}}(\vec{r}) = \sum_{\{\vec{G}\}} b_{\vec{G}}(\vec{k}) e^{i(\vec{k} + \vec{G} + \vec{G}')}, \quad (2.51)$$

where  $\{\vec{G}\}$  are the reciprocal lattice vectors (the expansion is possible due to its periodicity). We can always choose  $\vec{G}'$  such that  $\vec{k}' = \vec{k} + \vec{G}'$  lies in the first Brillouin zone and call  $b_{\vec{G}}(\vec{k}) \equiv a_{\vec{G}+\vec{G}'}(\vec{k})$ . This gives us

$$\psi_{n\vec{k}'}(\vec{r}) = e^{i(\vec{k}' \cdot \vec{r})} u_{n\vec{k}'}(\vec{r}). \quad (2.52)$$

Now  $\vec{k}'$  lies in the first Brillouin zone and the band index  $n$  indicates the act of restriction.

To see why it is good to do such a restriction, we have to understand the conservation of crystal momentum. To understand why the index  $n$  is called the band index, we can look at the nearly free electron model in the lattice for illustrations.

In short, Bloch electrons with the same crystal momentum modulo  $2\pi/a$  can interact with each other. This is because unlike momentum itself, crystal momentum is originated from discrete translational symmetry rather than a continuous one. So instead of momentum conservation, we now only have the fact that the momentum of an X-ray photon is allowed to change by reciprocal lattice vector times  $\hbar$ . This is the crystal momentum conservation interpretation of the Laue condition [10]. Despite being different from the momentum, crystal momentum can behave similarly to momentum in many cases [10] [20]. For example, if we make wave packets out of Bloch waves, their group velocity is



given by

$$\vec{v}_k = \frac{1}{\hbar} \nabla_{\vec{k}} \epsilon(\vec{k}).$$

For nearly free electrons in lattice with weak periodic potential, we can take two functions with degenerate energy in empty lattice states as our basis to diagonalize the Hamiltonian [21]. This results in a slight split in the original empty lattice bands wherever degeneracies happen.

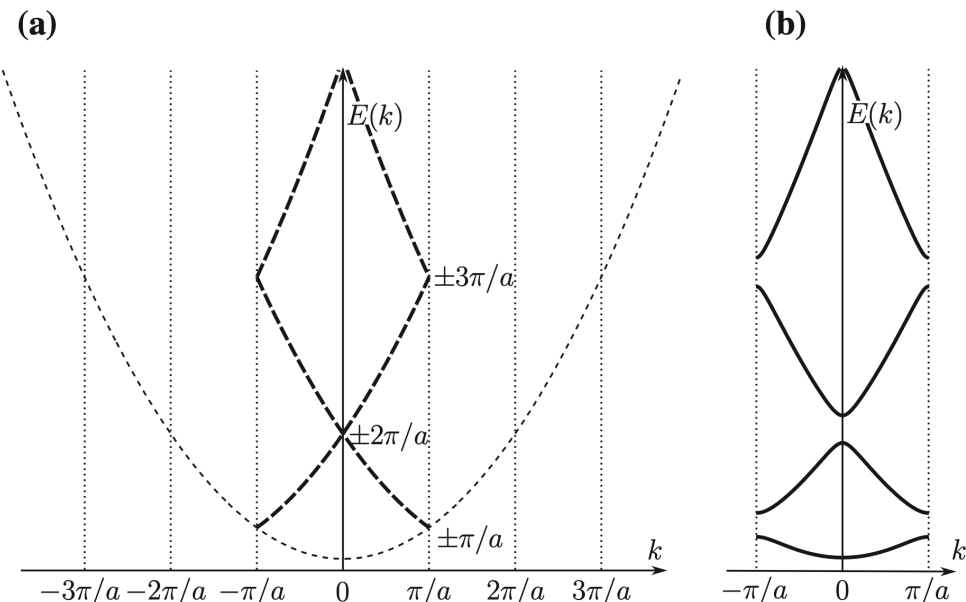


Figure 2.1: Band splitting of nearly free electrons [21]. (a) Band structure of the empty lattice. (b) Band structure of nearly free electrons.

The splitting implies electron in one band cannot move to another unless it absorbs energy and jumps through the discontinuous gap. The originally folded bands now have a transition-forbidden meaning that justifies the fact we call the folding index band index.

From the Bloch theorem and the crystal momentum, we know the origin of the Brillouin zone and why it is desirable to do the band analysis in it. The following sections will include the band structure of the target materials as well as an analysis of them.



## 2.4.2 Hohenberg-Kohn theorem, Kohn-Sham equation, and exchange-correlation energy

To dramatically cut down the computational effort for obtaining ground state wave functions, some useful theorems are developed. I now introduce them mainly following these two references [10][21]. The first Hohenberg-Kohn theorem proof (by contradiction) that two ground state wave functions (say, for  $v_{ext}$  and  $v'_{ext}$  respectively) must be identical if the density operator expectation values for both wave functions are the same.

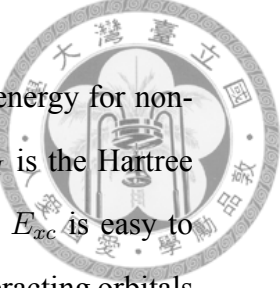
The second Hohenberg-Kohn theorem says the ground state energy can be expressed as a function of electron density. The energy functional is hence minimized by the true ground state density. To prove the second theorem, we first write the corresponding ground state wave function for a given density as  $|\Psi[n]\rangle$  (this one-to-one correspondence is the result of the first theorem). The total energy is then

$$E[n] = \langle \Psi[n] | T + U | \Psi[n] \rangle + \int d\vec{r} v_{ext}(\vec{r}) n(\vec{r}). \quad (2.54)$$

Since the one-to-one correspondence  $|\Psi[n]\rangle \leftrightarrow n(\vec{r})$  requires both the wave function and density be the ground state wave function and ground state density of some  $v_{ext}$ , not all densities are allowed to be in the domain of the functional. The densities have to really correspond to the ground state density of some  $v_{ext}$ . These kinds of densities are said to be  $V$ -representable. We can relax the  $V$ -representable condition to  $N$ -representable (the density corresponds to some  $N$ -electron density that is not necessarily the ground state). In the following discussion, we assume the densities we encounter are at least  $N$ -representable.

Kohn and Sham proposed we can look at a non-interacting system (presumably with a different  $v_{ext}$ ) that has the same ground state density as the interacting system (assume the existence of such correspondence). The energy functional would be easy to write down and the only difficulty is left in the exchange-correlation potential

$$E_{int}[n] = T_S[n] + E_H[n] + E_{xc}[n], \quad (2.55)$$



where  $E_{int}$  is the true interacting energy functional,  $T_S[n]$  is the kinetic energy for non-interacting ground state (Slater determinant of Kohn-Sham orbitals),  $E_H$  is the Hartree energy and  $E_{xc}$  is the exchange-correlation energy. Every term expects  $E_{xc}$  is easy to calculate and we can minimize the total energy with respect to the non-interacting orbitals to get Kohn-Sham equations.

$$\left[ -\frac{\hbar^2 \nabla^2}{2m} + v_{ext}(\vec{r}) + v_H(\vec{r}) + v_{xc}(\vec{r}) \right] \varphi_i(\vec{r}) = \varphi_i(\vec{r}). \quad (2.56)$$

The  $\varphi_i$  are the Kohn-Sham orbitals for the non-interacting corresponding system.

The exchange-correlation potential can be approximated by functional of  $n(\vec{r})$  or functional of both  $n(\vec{r})$  and  $\nabla n(\vec{r})$  and they are called local-density approximation (LDA) and generalized gradient approximation (GGA) potential respectively. The fact that we can do these approximations in the exchange-correlation term can be supported by several observations. First, the exchange integral operator for homogenous free electron gas can be well-approximated by local density potential [21]. Second, the exchange-only potential  $V_x[n(\vec{r})]$  is proportional to  $[n(\vec{r})]^{1/3}$  for Hartree-Fock-Slater approximation [21]. One can also see in a phenomenological way that LDA and GGA are sufficient in many cases except in strongly-correlated systems. We will use the obtained Kohn-Sham orbitals as the ground state orbitals of the material to further calculate physical properties.

## 2.5 Computational methods

### 2.5.1 Electronic structure

The *ab initio* calculations are done using the Vienna *ab initio* simulation package (VASP) [22] with the projector-augmented wave (PAW) method [23]. We use generalized gradient approximation (GGA) parametrized by the Perdew-Burke-Ernzerhof (PBE) formula [24] as the exchange-correlation potential. For valence electron configurations used, La, Al, Ge, Cu, Mn, As are  $5s^2 5p^6 5d^1 6s^2$ ,  $3s^2 3p^1$ ,  $3d^{10} 4s^2 4p^2$ ,  $3d^{10} 4s^1$ ,  $3d^6 4s^1$ ,  $4s^2 4p^3$  respectively. The energy cutoff is 500 eV and 400 eV for LaAlGe and CuMnAs respectively. The



structures of the two crystals are both taken from the experimental data [25][26][27]. For  $k$ -points sampling, the self-consistent electronic structure uses  $\Gamma$ -centered  $k$ -point meshes of  $16 \times 16 \times 16$  and  $9 \times 15 \times 9$  respectively for LaAlGe and both AFM structure of CuMnAs with tetrahedron method [28]. The band is drawn along high symmetry line using Gaussian smearing.

### 2.5.2 Optical conductivity

To understand nonlinear optics, I also calculate linear optical conductivity. It is the first-order effect and the formulae show some overlap that will be explained later in this section. Three generally independent components are calculated using the Kubo formula within linear-response theory [15][21]. The conductivity at each  $k$ -point is

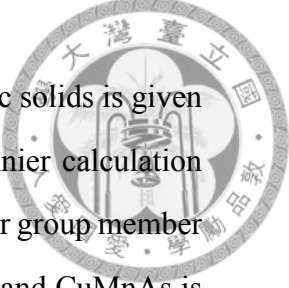
$$\sigma_{\mathbf{k},\alpha\beta}^H(\omega) = \frac{-\pi e^2}{\hbar\Omega_c} \sum_{n,m} (f_{m\mathbf{k}} - f_{n\mathbf{k}})(\varepsilon_{m\mathbf{k}} - \varepsilon_{n\mathbf{k}}) A_{nm,\alpha}(\mathbf{k}) A_{mn,\beta}(\mathbf{k}) \bar{\delta}(\varepsilon_{m\mathbf{k}} - \varepsilon_{n\mathbf{k}} - \hbar\omega), \quad (2.57)$$

where  $\bar{\delta}$  is the broadened delta-function,  $\hbar\omega$  is the photon energy,  $\varepsilon_{n\mathbf{k}}$  is the  $n$ -th band energy at point  $\mathbf{k}$ , and we will get the conductivity after integral over Brillouin zone. Berry connection ( $\propto$  dipole matrix elements)  $A_{nm,\alpha}(\mathbf{k})$  are obtained from the Wannier gauge formalism after we obtain the Wannier functions [29]. We notice the  $A_{nm,\alpha}(\mathbf{k}) A_{mn,\beta}(\mathbf{k})$  in linear optical conductivity is the transition amplitude that also appears in bulk photovoltaic effect.

Although I only study the real part of the linear conductivity in sections 4.3 and 5.2, it is possible to connect it with the imaginary part. The imaginary part of optical conductivity is associated with the real part of the dielectric constant which describes the energy loss. It can be obtained via the Kramers-Kronig relations [21].

### 2.5.3 Matrix elements used in post-Wannier calculation

In the nonlinear optical conductivity calculation, the dipole matrix elements  $\langle \mathbf{k}n | r^a | \mathbf{k}n' \rangle$ , velocity matrix elements  $\langle \mathbf{k}n | v^a | \mathbf{k}n' \rangle$ , and the generalized derivative  $r_{nm,a}^c$  are calculated from the Wannier framework [29][30]. The needed Wannier functions are obtained using



Wannier90-3.1.0 [15]. The code for the calculation of BPVE for magnetic solids is given by Professor G.-Y. Guo. Modifications of subroutines within PostWannier calculation including berry.F90, kslice.F90, and kpath.F90 are made by me and former group member Kun-Han Lu. The quasiparticle lifetime for semimetals such as LaAlGe and CuMnAs is taken to be 0.01 eV.

### 2.5.4 Formulae used in post-Wannier calculations

To test the validity of my code, I calculate Berry curvature using a formula in accordance with that mentioned in Wanneir document [15]

$$\Omega_{\alpha\beta}(k) = 2 \sum_n^{\text{occ}} \sum_{m \in \text{all}} \text{Im} [r_{nm}^\alpha r_{mn}^\beta]. \quad (2.58)$$

As for geometric quantities, we use the formulae given in section 2.3. For quantum metric, it is

$$g_{ba}(k) = \sum_{n \in \text{occ}} \sum_{m \in \text{unocc}} \text{Re} [r_{nm}^b r_{mn}^a]. \quad (2.59)$$

Quantum geometric connection gives both the Christoffel symbol of the first kind

$$\Gamma_{bca} = \text{Re}[C_{bca}] \approx \text{Re} \left[ \sum_{n \in \text{occ}} \sum_{m \in \text{unocc}} r_{nm}^b r_{mn,c}^a \right], \quad (2.60)$$

and the symplectic Christoffel symbol

$$\tilde{\Gamma}_{bca} = -\text{Im}[C_{bca}] \approx -\text{Im} \left[ \sum_{n \in \text{occ}} \sum_{m \in \text{unocc}} r_{nm}^b r_{mn,c}^a \right]. \quad (2.61)$$

Again, the approximation here indicates the neglect of the virtual transitions mentioned in [2]. Note also this approximated expression for Christoffel symbol of the first kind and symplectic Christoffel symbol correspond to the metric connection and symplectic connection respectively in [31]. The calculated Christoffel symbols in the  $k$ -path analysis in sections 4.5.3 and 5.4 are the approximated ones listed here, and I use the terminologies and equations in [31] to explain the results. I implement these formulae into post Wannier framework.





# Chapter 3

## Overview of physical properties of studied materials LaAlGe and CuMnAs

### 3.1 LaAlGe

#### 3.1.1 Introduction and current state in research

Lanthanum aluminum germanide (LaAlGe) is a 3D crystal that has been synthesized experimentally and with first principle predicted nonmagnetic ground state [25][32][33]. It is also verified both experimentally and theoretically a Weyl semimetal containing both type one and type two Weyl points [32]. Previous studies on LaAlGe include structural study in the 1990s [25] [26] and a combination of first principle and ARPES study in the 2010s due to raising interests in Weyl semimetals and Weyl fermion[32] [33].

#### 3.1.2 Structure, symmetry, and Brillouin zone of LaAlGe

Bulk LaAlGe belongs to space group I4<sub>1</sub>md (number 109), which has a body-centered tetragonal unit cell containing four lanthanum, aluminum, and germanium atoms. The primitive cell is a triclinic cell with two of each kind of atom. The transformation formula is



$$\begin{pmatrix} \vec{a_1} \\ \vec{a_2} \\ \vec{a_3} \end{pmatrix} = \begin{pmatrix} -\frac{a}{2} & \frac{a}{2} & \frac{c}{2} \\ \frac{a}{2} & -\frac{a}{2} & \frac{c}{2} \\ \frac{a}{2} & \frac{a}{2} & -\frac{c}{2} \end{pmatrix} \begin{pmatrix} \hat{x} \\ \hat{y} \\ \hat{z} \end{pmatrix},$$

where  $\vec{a}_i$  is the primitive basis vectors and  $\hat{x}_i$  is the Cartesian basis. Below I show the conventional unit cell where we can see the full symmetry more easily, and a top view to demonstrate the  $S_{4z}$  screw rotation axis.

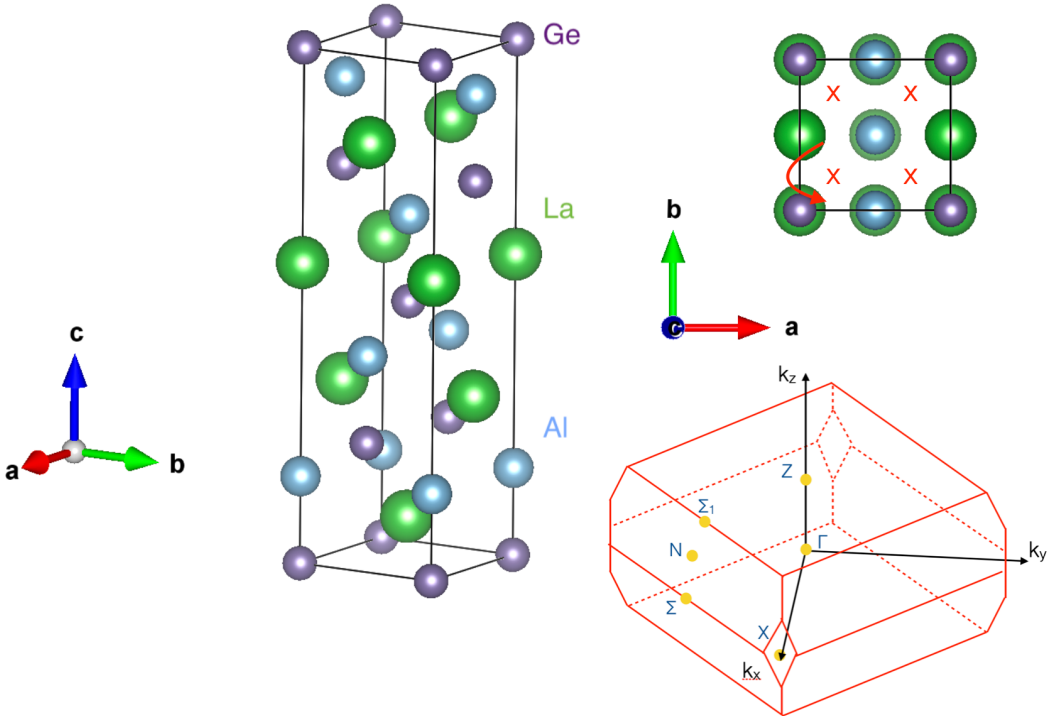
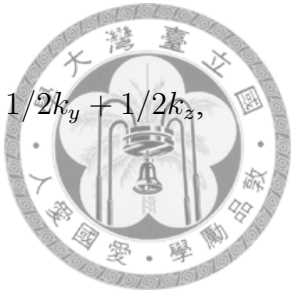


Figure 3.1: Conventional unit cell for body-centered tetragonal LaAlGe (left), top view of the structure with  $S_{4z}$  screw rotation axis and the Brillouin zone (bottom right).

The experimental lattice constants has several reports ranging from  $a = b = 4.336\text{\AA}$  and  $c = 14.828\text{\AA}$  [25] to  $a = b = 4.341\text{\AA}$  and  $c = 14.784\text{\AA}$  [26]. The lattice constant used in the calculation is  $a = b = 4.34(4)\text{\AA}$  and  $c = 14.81(2)\text{\AA}$ . Wyckoff positions are  $4a$  for all three kinds of atoms. The important symmetries here are four-fold screw rotation  $S_{4z}$ ,  $M_x$ , and  $M_y$ . The system has no inversion symmetry and hence is allowed to have second-order nonlinear optical effects.

The bottom right figure shows the Brillouin zone for this body-centered tetragonal crystal with the corresponding high symmetry points. The relation between reciprocal



lattice vectors  $\vec{b}_i$  and  $\vec{k}_i$  is  $b_1 = -1/2k_x + 1/2k_y + 1/2k_z$ ,  $b_2 = 1/2k_x + 1/2k_y + 1/2k_z$ ,  $b_3 = k_y$ .

## 3.2 CuMnAs

### 3.2.1 Introduction and current state in research

Copper manganese arsenide (CuMnAs) is a 3D crystal with both experimental and first principle data that claim its antiferromagnetic (AFM) ground state [34][35]. Though the AFM ground state is robust up to above room temperature [34], the AFM local magnetic moment direction has no experimental conclusion. There are papers reporting experimental b-axis local moment [36], the theoretical prediction of c-axis local moment [35] as well as a more complex local AFM moment due to the unresolved experimental conclusion, energetically closed DFT ground state energy and the fact that the other compound in the family, CuMnSb, is a Heusler AFM material [34]. It is for this reason we choose to study both the c-axis and b-axis AFM structure of CuMnAs. I am curious about what differences will occur specifically regarding phenomena related to nonlinear optics. If there exist interesting differences one can either use it to detect the magnetic ground state of the material or tune the magnetic ground state as a control to see the change in BPVE effects.

The c-axis CuMnAs have their local magnetic moment parallel to the c-axis, yet there exists another AFM structure that has the same kind of AFM structure (Mn atoms with the same b-axis coordinate having an opposite local moment) but with the local moment parallel to the b-axis. There are still debates in the experimental ground state of this CuMnAs compound whether being AFM along c-axis or b-axis and the first principle calculation result has close ground state energy for these two configurations.

### 3.2.2 Structure, symmetry, and Brillouin zone of CuMnAs

Below I show the conventional unit cell for c-axis AFM CuMnAs, a top view along the b-axis is shown to demonstrate the  $S_{2z}$  symmetry and the Brillouin zone. All atoms have



Wyckoff position  $4c$  if we neglect local magnetic momentum, and they possess site symmetry .m..

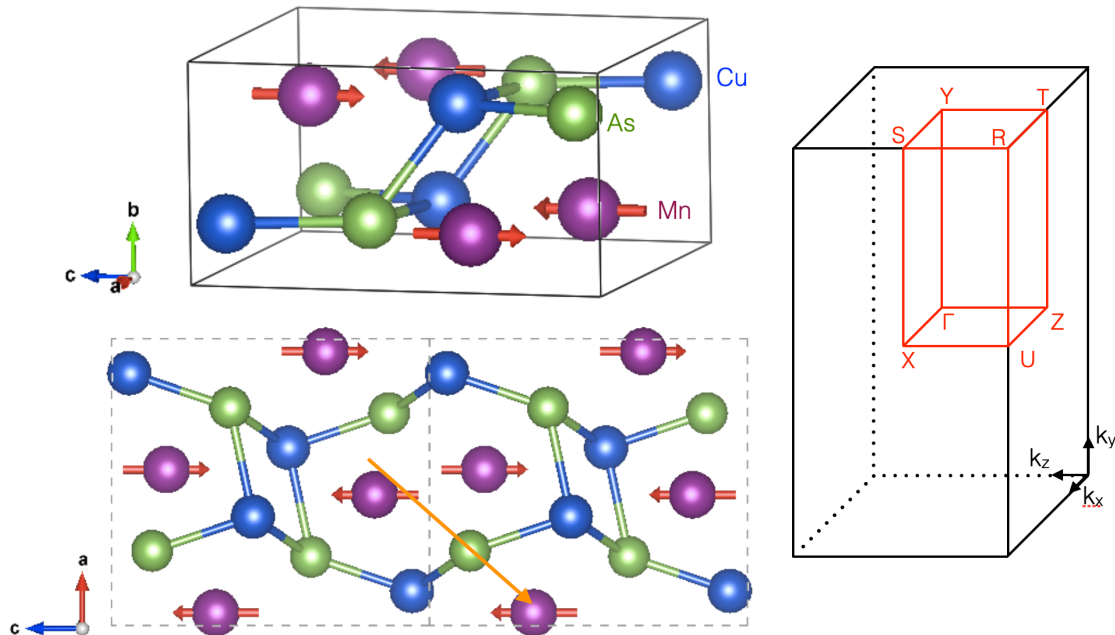


Figure 3.2: Conventional unit cell for c-axis AFM CuMnAs (top left), b-axis view to demonstrate the  $S_{2z}$  symmetry (bottom left) and the Brillouin zone (right).

We also study the b-axis AFM configuration with the same atom positions in the unit cell. In the symmetry aspect, it is important to notice that both c- and b-axis CuMnAs possess parity-time (PT) symmetry yet only c-axis AFM CuMnAs have  $S_{2z}$  symmetry while b-axis AFM CuMnAs break the  $S_{2z}$  symmetry. This will not only cause the difference in nonzero conductivity tensor components but will also cause c-axis AFM CuMnAs to possess Dirac points protected by this symmetry and the Dirac point is gapped in the case of b-axis AFM CuMnAs [35].

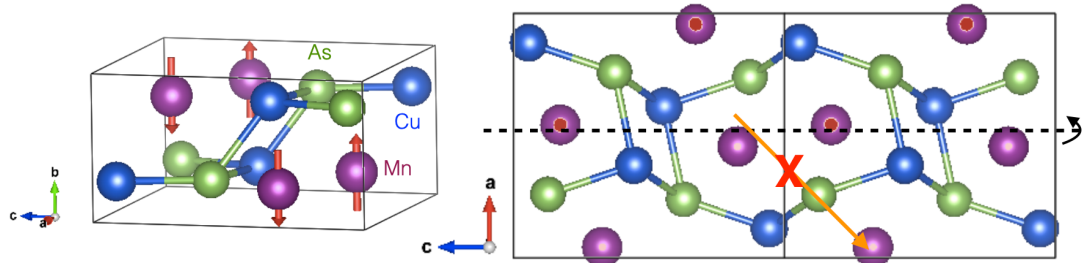


Figure 3.3: Conventional unit cell for b-axis AFM CuMnAs (left), b-axis view to demonstrate the breaking of  $S_{2z}$  symmetry (right).



# Chapter 4

## Bulk photovoltaic effect of nonmagnetic Weyl semimetal LaAlGe

### 4.1 Electronic structure of LaAlGe

As mentioned in chapter 3, LaAlGe has been experimentally synthesized and we use the experimental structure here to do the electronic calculations. Calculation details are listed in section 2.5. The DFT and Wannier band structure are given below. We can see from the band structure that LaAlGe is a semimetal, having few states crossing the Fermi level. We also notice a wide gap at the high symmetry point Z with an energy difference larger than 2 eV. Flat bands occur at around 2 eV above the Fermi level and are dominated by itinerate La f-orbitals.

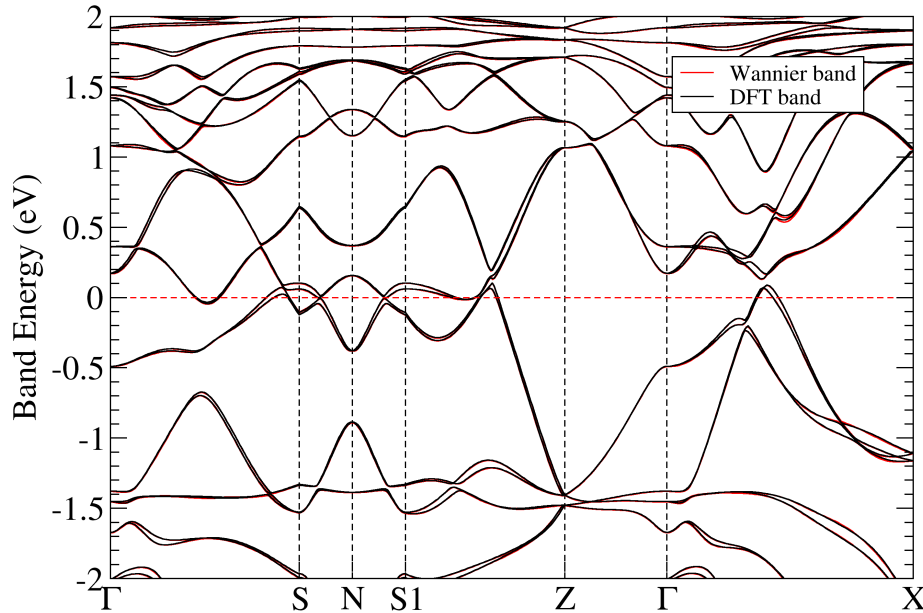


Figure 4.1: DFT and Wannier band of nonmagnetic bulk LaAlGe. The Fermi level is shifted to 0 eV.

## 4.2 Weyl point structure of LaAlGe

In this section, we look into the Weyl point structure of LaAlGe, specifically, where different types of Weyl points located and what are their energy-momentum dispersion relations. This will be closely related to the enhancement and dominant regions of several quantities that will be discussed later. There are both type-I and type-II Weyl points in LaAlGe, and due to the characteristic of the inclination of these two types of Weyl point, they will also cause a different effect on the second-order conductivity that will be studied later. The location of Weyl points is calculated using the WannierTool package [37].

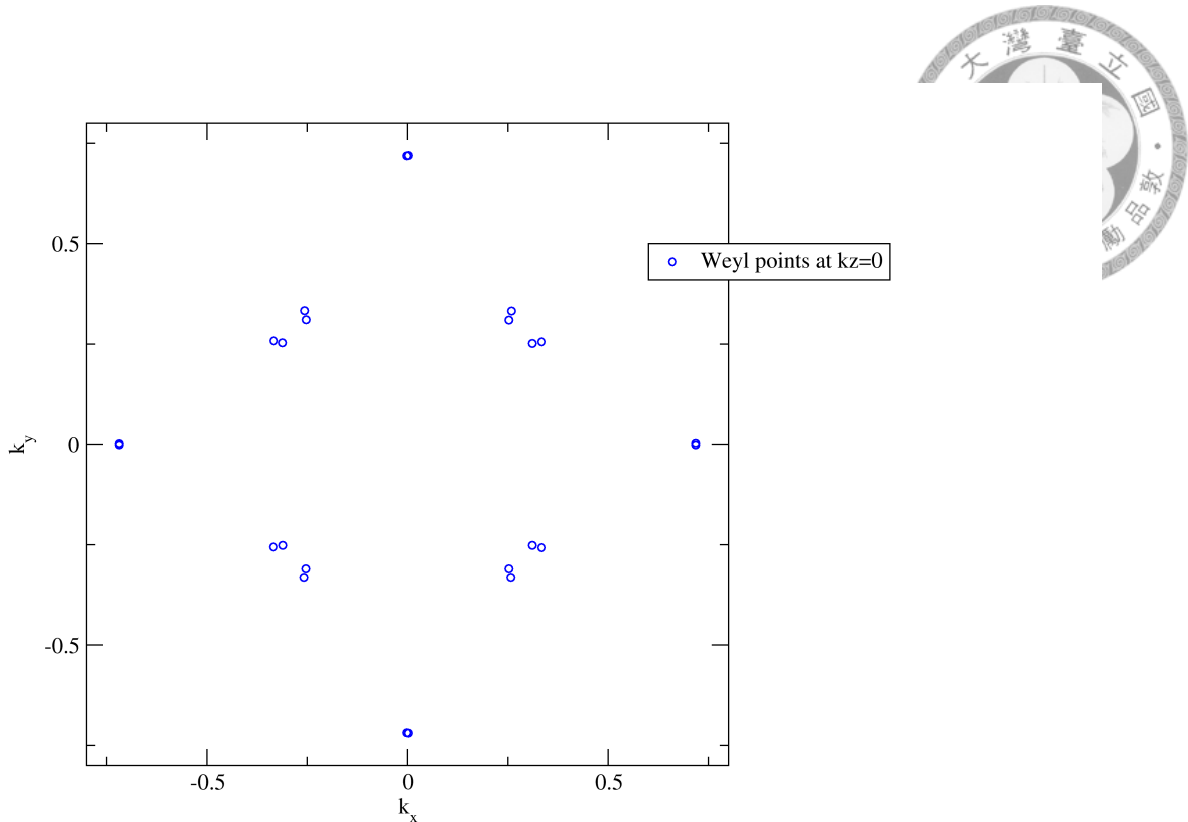


Figure 4.2: Weyl points in the  $k_z=0$  plane of Brillouin zone. It can be seen from the schematic diagram below that this plot contains  $W_1$  and  $W_3$  that fall around 60 and 110 meV above the Fermi level respectively.

Unlike Dirac points that usually located on high symmetry lines within the Brillouin zone, Weyl points can and generally will locate off the high symmetry lines. So if we want to find their positions in the  $k$ -space and further study their energy-momentum dispersion relation or chirality, we will have to first scan across the Brillouin zone looking for band crossing and using the obtained locations to plot out the band dispersion for each crossing points.

The above figure contains the locations of Weyl points that are labeled  $W_1$  and  $W_3$  and they both belong to type-I Weyl point. The type-II Weyl points are located at  $k$ -plan where  $k_z$  not equal to zero. The dispersion relation in the vicinity of these three types of Weyl points will be inspected now. I show here my calculation results and the schematic diagram of  $W_1$ ,  $W_2$ ,  $W_3$  taken from [32].

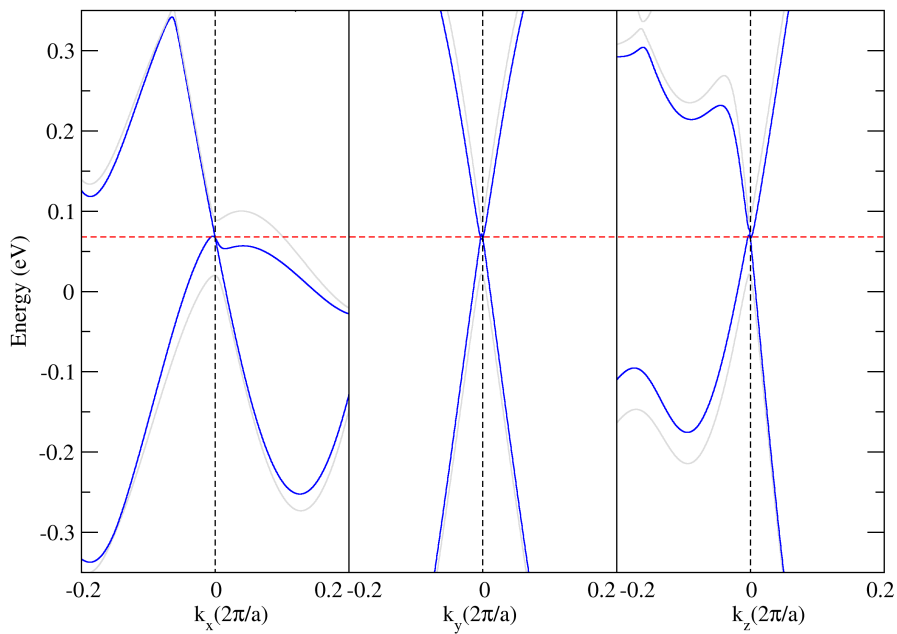


Figure 4.3: Dispersion relation near  $W_1$ . The x-axis label is the same for the following two graphs.

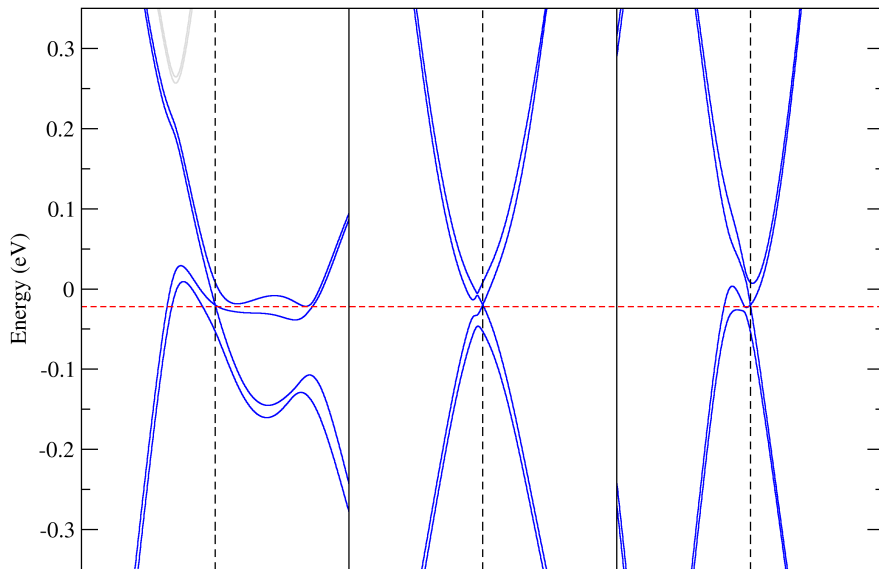


Figure 4.4: Dispersion relation near  $W_2$ . The x-axis label is the same as that of  $W_1$  graphs.

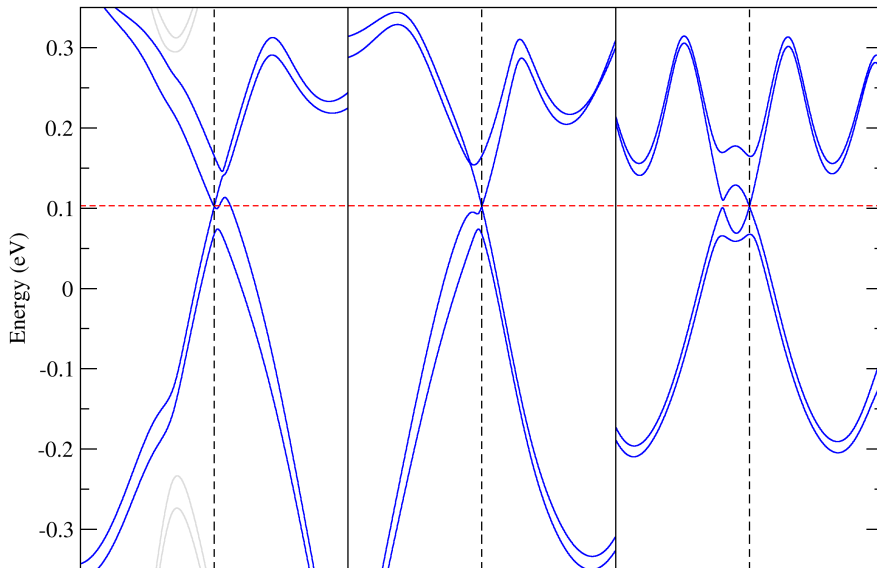


Figure 4.5: Dispersion relation near  $W_3$ . The x-axis label is the same as that of  $W_1$  graphs.

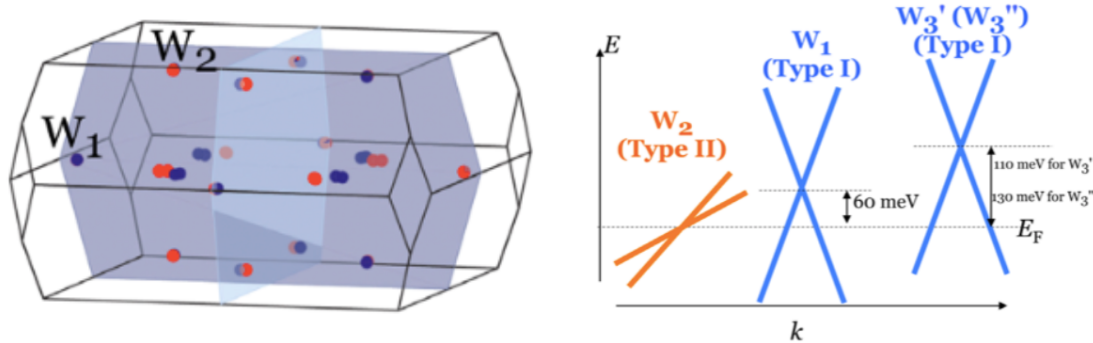


Figure 4.6: Schematic diagram of  $W_1$ ,  $W_2$ ,  $W_3$ , and their dispersion relation and location inside Brillouin zone.

### 4.3 Joint density of states and linear optical conductivity

In order to understand the second-order optical response, we first inspect the first-order optical conductivity as well as the joint density of states (JDOS). The JDOS considers only the probability of transition in the joint probability sense. Namely the probability of one electron initially at the valence band and not at the conduction band that has a  $\hbar\omega$



energy difference. It doesn't take the matrix elements into account. The first-order optical conductivity takes into account the matrix element of first-order electric dipole interaction as the perturbation. By studying these two quantities we get to know whether the nonlinear response originated from the JDOS, the first-order response, or second-order quantities such as the velocity difference and the shift vector. If the JDOS and the first-order response are small around the BPVE conductivity peak position, we know the dominating mechanism is purely second-order. If the first-order conductivity is suppressed, the second-order effect can be singled out and better observed.

For LaAlGe, as we can see from the figure below, the JDOS and optical conductivity are indeed small in the low-energy region. For JDOS, the low values in the low-energy region simply reflect the fact that LaAlGe is a semimetal with a low density of states near the Fermi level. As for linear optical conductivity, it is also low in the low-frequency region and has a broad peak at around 0.4 eV. The  $k$ -grid used is  $80 \times 80 \times 110$ .

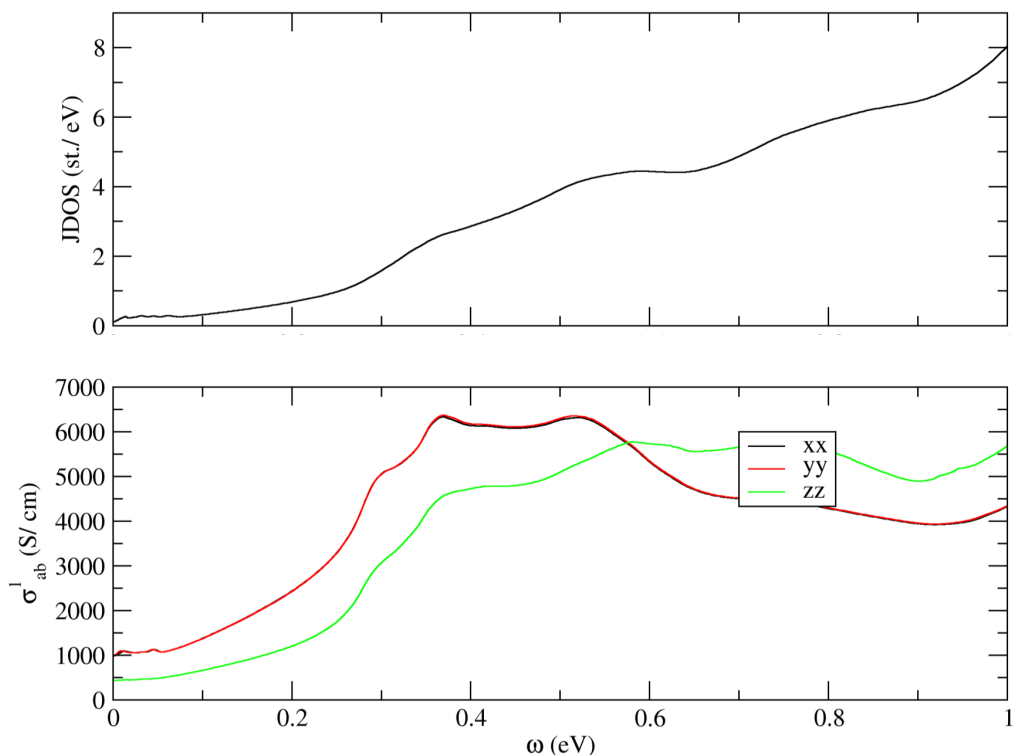


Figure 4.7: Joint density of states and first-order optical conductivity of LaAlGe.



## 4.4 Shift and injection current conductivity spectrum

For LaAlGe, since there are three types of Weyl points with different energy away from the Fermi level, we will first look at the calculation result of leaving the Fermi level intact as the self-consistent calculation result. Next, we will shift the Fermi level to the energy values of  $W_1$ ,  $W_2$ , and  $W_3$  to see whether there is an enhancement of peak value, lowering of the peak position, or sign change of peaks. We look at the circular injection current first.

For  $\mu = E_F$ , there are two main peaks, one at a lower frequency (around 0.05 eV) regime with a sharper peak shape and negative value; the other is located around 0.5 eV with a broad peak shape and positive value. Also, the  $\sigma_{xxz}$  and  $\sigma_{yyz}$  component though independent in the tensor symmetry analysis, looks almost identical. This may be explained by the  $S_{4z}$  symmetry that exists in the material: it can be seen as effective  $C_4$  symmetry if we project in the  $\hat{z}$  direction, and  $C_4$  maps  $\hat{x}$  to  $\hat{y}$ . When we shift the chemical potential to  $E_{W_1}$ , the lower energy peak changes sign from negative to positive and is slightly enhanced in magnitude. However, the peak shape seems to be split and hence broadened. On the other hand, the higher energy peak is left almost intact. When the chemical potential is shifted to  $E_{W_2}$  which is the closest to the Fermi level, the circular injection spectrum only changes slightly in the low energy peak where it split slightly. Finally, we shift the chemical potential to  $E_{W_3}$ . The low energy peak again changed sign and the splitting of the peak is even more prominent now.

Comparing the four spectrums, we see the most obvious sign change in the low energy region happens when we shift the chemical potential to  $E_{W_1}$ . As can be seen in the following plot, this also happens for the shift current. I try to see the origin of this sign change by drawing the contribution of shift current and symplectic Christoffel symbol along  $k_x$ ,  $k_y$ , and  $k_z$ .

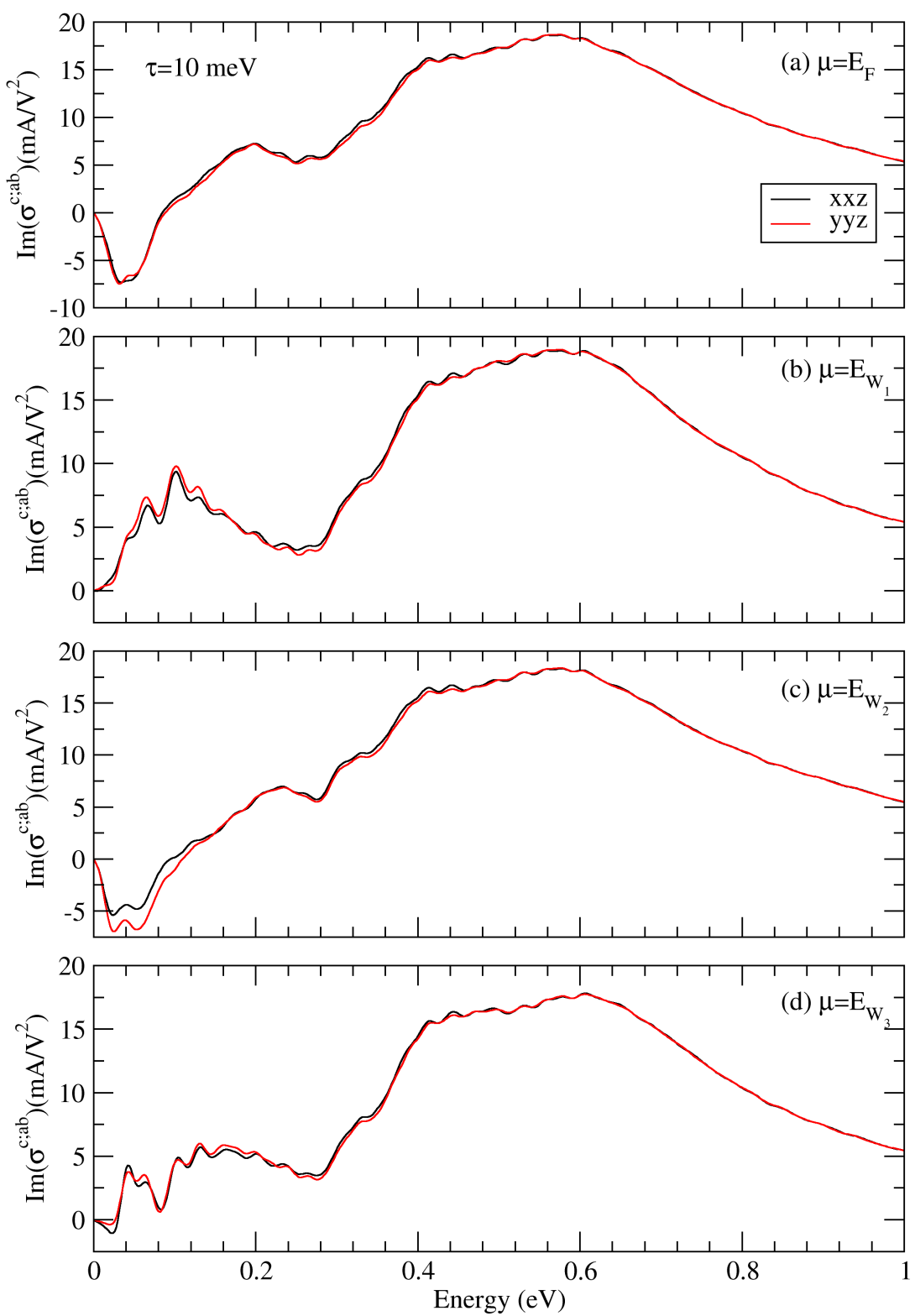
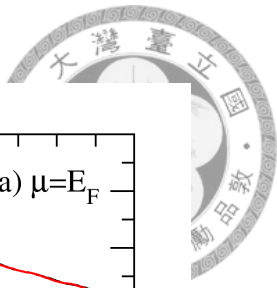


Figure 4.8: Independent component of circular injection current in LaAlGe with chemical potential equal to (a)  $E_F$ , (b) shifted to  $E_{W_1}$ , (c)  $E_{W_2}$  and (d)  $E_{W_3}$ .

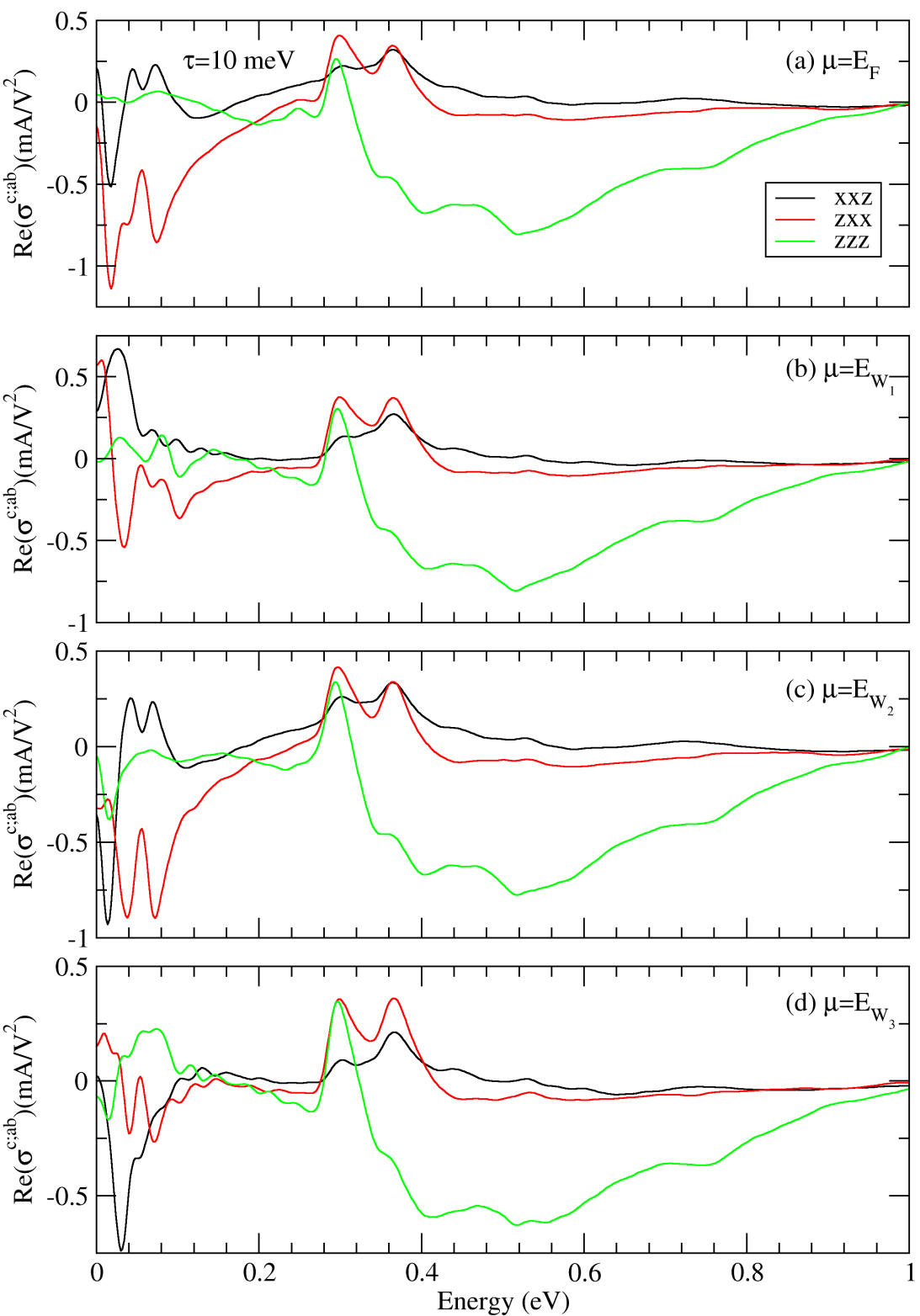
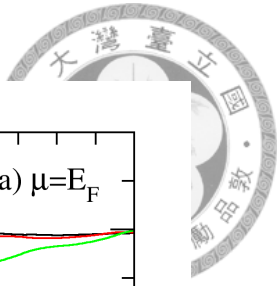
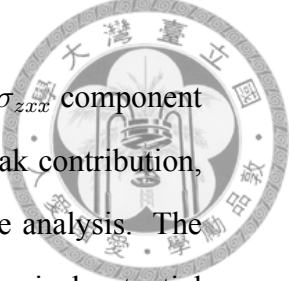


Figure 4.9: Independent component of linear shift current in LaAlGe with chemical potential equal to (a)  $E_F$ , (b) shifted to  $E_{W_1}$ , (c)  $E_{W_2}$  and (d)  $E_{W_3}$ .

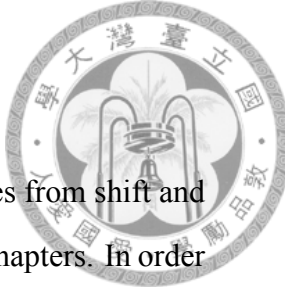
Now let us focus on the linear shift current of LaAlGe. For  $\mu = E_F$ , we notice the  $\sigma_{xxz}$  and  $\sigma_{zxx}$  component has a huge low energy peak at the same peak position. When



shifted to  $E_{W_1}$ , the previously-mentioned two peaks change sign yet the  $\sigma_{zxx}$  component peak is not dropped to zero at zero frequency. To better separate the peak contribution, we choose the low energy peak of  $\sigma_{xxz}$  component to do further  $k$ -slice analysis. The peak is located at 0.026 eV for  $\sigma_{xxz}$  component. When we shift the chemical potential to  $E_{W_2}$ , the  $\sigma_{zzz}$  component is largely enhanced with a peak position close to that of the  $\sigma_{xxz}$  component. The  $\sigma_{zxx}$  component has two large peaks after  $\sigma_{xxz}$  causing three peaks that are comparable in magnitude appearing at low energy regime. The peak is located at 0.014 eV for  $\sigma_{xxz}$  component. Finally at  $E_{W_3}$ , the  $\sigma_{xxz}$  component completely dominant and  $\sigma_{zxx}$  shrinks to the same magnitude as  $\sigma_{zzz}$  component. The peak is located at 0.03 eV for  $\sigma_{xxz}$  component. To summarize, the enhancement of low energy peak is most significant in  $\sigma_{xxz}$  when the chemical potential is shifted to  $E_{W_2}$ . For the sign change of low energy peak, we see  $\sigma_{xxz}$  changes sign for  $\mu = E_{W_1}$ . We thus choose this particular component to do further  $k$ -path studies.

## 4.5 $k$ -path and $k$ -slice analysis of conductivity and geometric quantities

To understand the origin of the conductivity peak, one way is to look into the Brillouin zone and see which region contributes the most. We can then associate the dominant region with the band structure and see what kind of band structure can possibly create a large photovoltaic response. This is good if the dominant region is indeed caused by points located on the high symmetry line and is due to characteristics of the band. However, there is also the possibility that the dominating region is not on the high symmetry line and is hard to see from the  $k$ -path analysis. We use  $k$ -slice analysis in this circumstance. Another benefit of doing the  $k$ -slice analysis is we will be able to see the symmetry or asymmetry of the studied quantities that are not manifested in spectrum nor  $k$ -path analysis.



### 4.5.1 $k$ -slice analysis validity check: Berry curvature

We modify the PostWannier code to calculate  $k$ -slice of various quantities from shift and injection current to the four geometric quantities mentioned in previous chapters. In order to make sure the code is valid we have to test it with the quantity that we can already calculate using Wannier90-3.1.0 which is Berry curvature  $k$ -slice. Below I show four plots where the upper two graphs are using the same color map while the bottom two graphs use another. The two graphs on the left-hand side are the results calculated by my code whereas the ones on the right-hand side are the results of the Wannier built-in function. The kmesh used is 100x100.

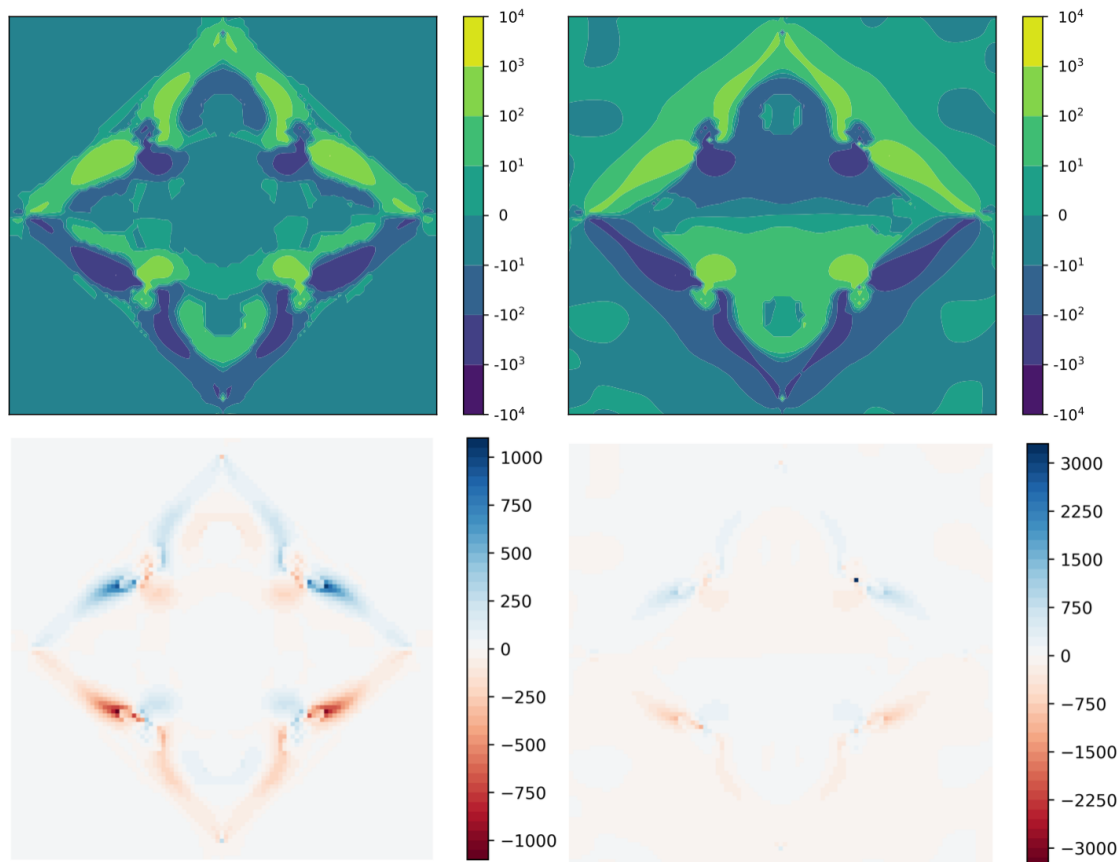
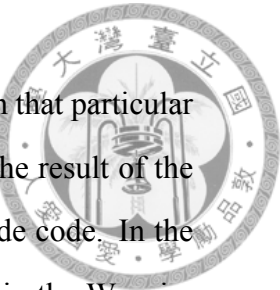


Figure 4.10: Berry curvature  $k$ -slice of LaAlGe on X-Y plane containing  $\Gamma$  point. Upper left: color map No.1, my code; Upper right: color map No.1, Wannier built-in function; bottom left: color map No.2, my code; bottom right: color map No.2, Wannier built-in function.

We can see there is an extreme value point in the Wannier built-in result with color map No.2 that is without any symmetry and will change its BZ location when I further increase



the number of  $k$ -points. I think it is unphysical and I compare it again with that particular data point taken out. The result shows good agreement in my code and the result of the Wannier built-in function. We then conclude the validity of the homemade code. In the homemade code, the Berry curvature is calculated by equation 2.58 within the Wannier framework [29]. For Wannier built-in function, it uses Eq.27 from [30].

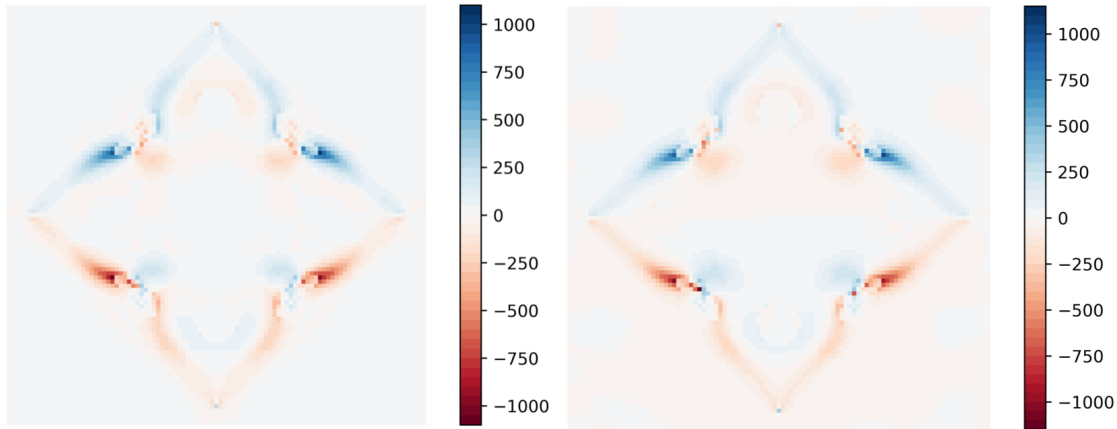


Figure 4.11: Berry curvature  $k$ -slice of LaAlGe on X-Y plane containing  $\Gamma$  point. Left: my code; right: Wannier built-in function with extreme value point taken out.

#### 4.5.2 $k$ -slice analysis of circular injection conductivity and Berry curvature

We try to see the connection between the conductivity spectrum, Weyl point structure, conductivity  $k$ -slice, and geometric quantity  $k$ -slice here. For LaAlGe, we look at the circular injection current first. The conductivity  $k$ -slice is plotted at peak energy = 0.5 eV and both the spectrum and conductivity are calculated with the Fermi level shifted to  $E_{W_1}$ . We see the conductivity is dominant in the region connecting  $W_1$  and  $W_3$ , and around  $W_3$ , so we know the this peak originated from the combination of  $W_1$  and  $W_3$ , and the region connecting them. Since  $W_1$  and  $W_3$  are gap closing points with 60 and 100 meV above the Fermi level, we suspect the dominating lines connecting  $W_1$  and  $W_3$  are caused by states that are energetically close to the Fermi surface. When we compare the circular injection conductivity and Berry curvature  $k$ -slice, we notice the dominating region being largely overlapped. Despite the similarity in these two  $k$ -slice plots, the sign is different for two



square lines in the lower half. By inspecting the two-band formula that serves as a good approximation when the energy difference of the two crossing bands is much smaller than their energy difference with other bands, we see the explanation of this sign difference.

$$\sigma_{inj}^{c;ab} = -\tau \frac{2\pi e^3}{\hbar^2} \int_{\omega=\omega_{cv}} \frac{d^{d-1}k}{(2\pi)^d} (\hat{n} \cdot \hat{c}) Q_{ba} \quad (4.1)$$

If we take the imaginary part for both sides, it describes the relation between circular injection conductivity and Berry curvature. Since the tensor component we are plotting is  $\sigma_{xxz}$  which has a similar behavior as  $\sigma_{yyz}$ , the Berry curvature  $\Omega_{yz} = -\Omega_{zy}$  should indeed change sign when we go from the upper half to lower half  $k$ -slice so that after taking the inner product of  $\hat{n} \cdot \hat{c}$  ( $\hat{n}$  will be pointing outward along the square shape lines since we define it as the direction of positive  $\nabla E$ , and  $\hat{c}$  now equals  $\hat{y}$ ) the values of upper and lower plane add to each other rather than cancel out.

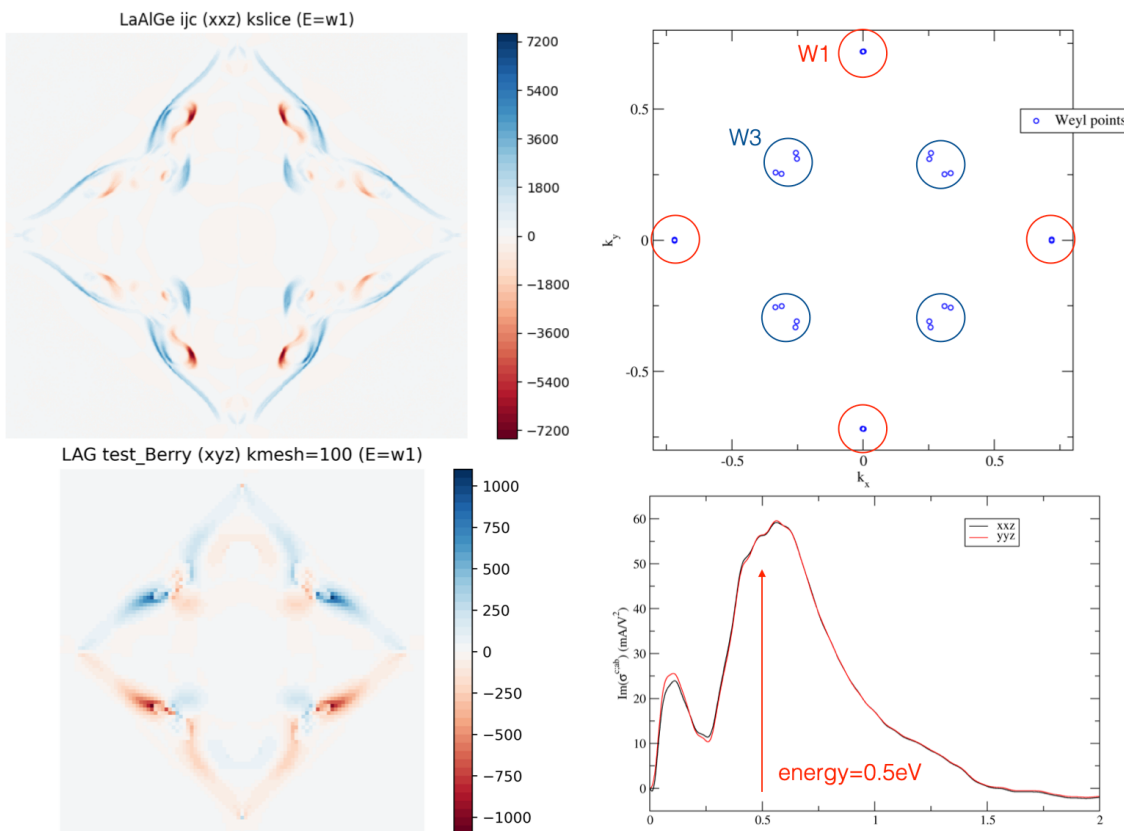


Figure 4.12: Circular injection conductivity and Berry curvature  $k$ -slice of LaAlGe on X-Y plane containing  $\Gamma$  point. Upper left: circular injection conductivity  $\sigma_{xxz} \approx \sigma_{yyz}$ ; Upper right: Weyl point structure; bottom left: Berry curvature  $\Omega_{yz}$ ; bottom right: circular injection conductivity spectrum with the selected peak pointed out.



### 4.5.3 $k$ -path analysis of linear shift conductivity and symplectic Christoffel symbol

In order to understand the origin of linear shift current and peak sign change in LaAlGe, I choose  $\sigma_{xxz}$  to study. According to [31], the shift current can be expressed as

$$\sigma_{shift}^{c;ab} = -\frac{\pi e^3}{2\hbar^2} \sum_{n,m} \int_k \delta(\omega - \omega_{mn}) f_{nm} i (C_{bca}^{mn} - (C_{acb}^{mn})^*), \quad (4.2)$$

with  $C_{bca}^{mn} = r_{nm}^b r_{mn,c}^a$ , and the imaginary part of  $C_{bca}^{mn}$  is the symplectic connection in [31]. When  $\mu = E_f$ , both the symplectic Christoffel symbol and the linear shift current are dominant around  $W_1$ . The original negative contribution around  $W_3$  vanishes and positive contributions around  $W_1$  emerge, this could be the reason for the previously mentioned sign change of  $\sigma_{xxz}$  peak.

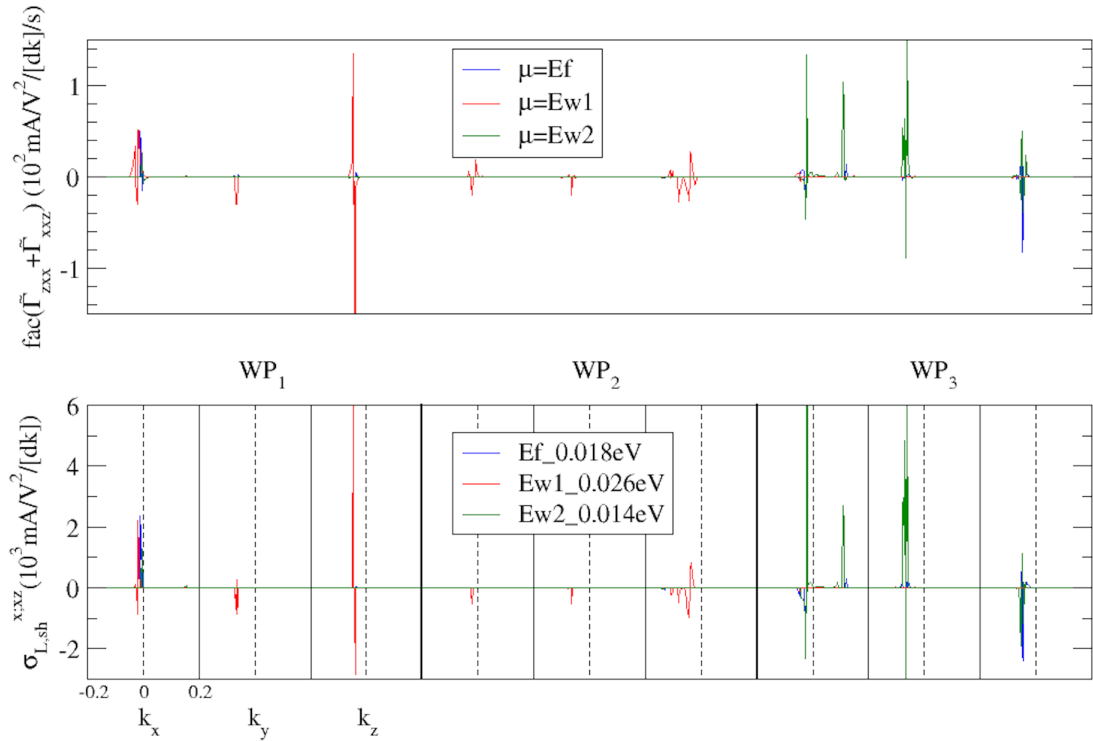


Figure 4.13:  $k$ -path of linear shift conductivity and symplectic Christoffel symbol ( $\tilde{\Gamma}$ ) in LaAlGe. Each plot contains  $k$ -path across three Weyl points:  $W_1$ ,  $W_2$ , and  $W_3$  from left to right. Within each Weyl point, the  $k$ -path run through it in  $k_x$ ,  $k_y$ , and  $k_z$  from left to right. Upper panel: addition of symplectic Christoffel symbol with  $\text{fac} = \pi e^3 / 2\hbar^2$ , the three colors represent setting  $\mu = E_f$ ,  $E_{W_1}$ , and  $E_{W_2}$  respectively. Lower panel: linear shift current, the three colors represent choosing the lowest peak frequency in  $\mu = E_f$ ,  $E_{W_1}$ , and  $E_{W_2}$ .



# Chapter 5

## Bulk photovoltaic effect of PT-symmetric antiferromagnetic Dirac semimetal CuMnAs

In this chapter, we examine CuMnAs with the local antiferromagnetic axis parallel to both c- and b-axis due to reasons mentioned in section 3.2. For each physical quantity, c-axis and b-axis AFM CuMnAs will be introduced side by side, allowing us to make the comparison more directly.

### 5.1 Electronic structure of c-axis and b-axis AFM CuM-nAs

First, we look at the electronic structure of the Dirac semimetal CuMnAs with a local antiferromagnetic axis parallel to the c-axis. We examine closely with  $\pm 1\text{eV}$  around the Fermi level. We have several observations here. First, the bands near the Fermi level are very clean, making it an ideal platform to study the semimetal-related phenomenon. Second, there is only one crossing along this high symmetry line that is not gapped by spin-orbit interaction, namely the crossing on X-U. This is due to the existence of  $S_{2z}$  symmetry possessed by the crystal structure as explained in this paper by Peizhe Tang



[35]. Thirdly, there are energetically close gaps around the midpoint of  $\Gamma$ -X and Z-X high symmetry lines and a highly dispersive structure around high symmetry point Z.

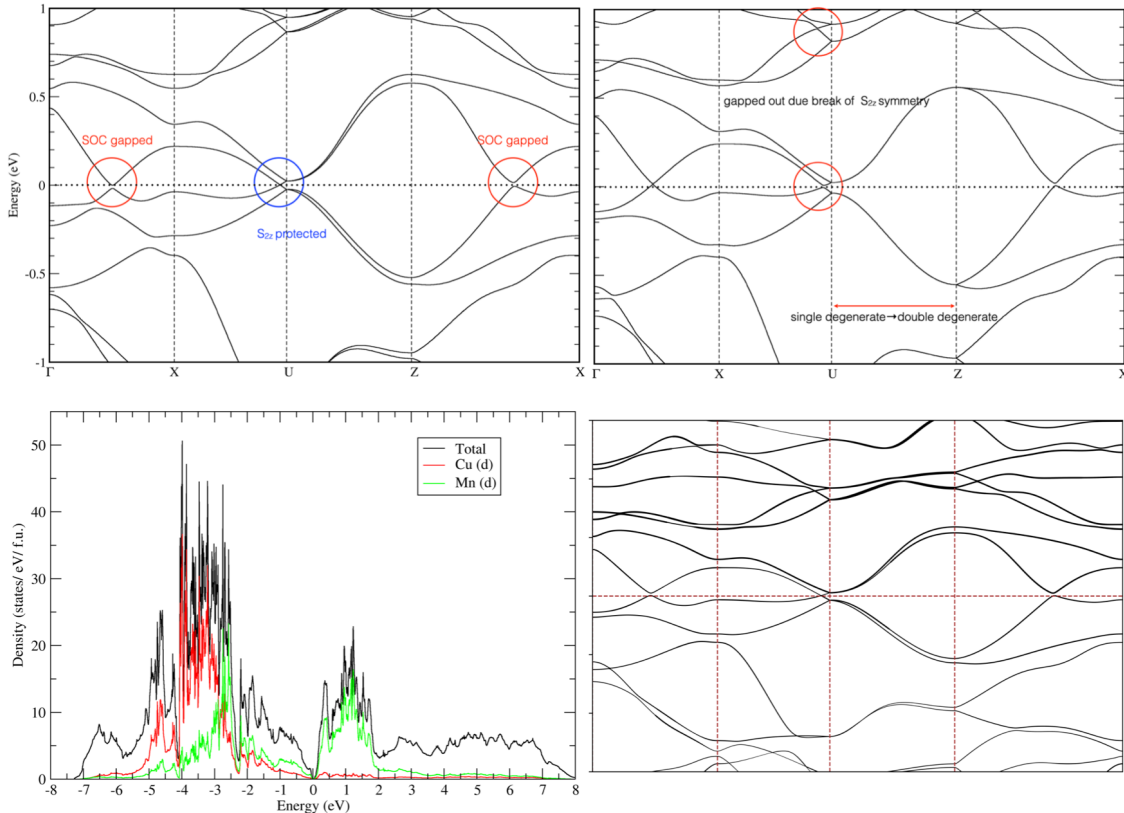


Figure 5.1: Upper left: band structure of c-axis and AFM CuMnAs. Upper right: band structure of b-axis and AFM CuMnAs. Lower left: partial density of states of c-axis and AFM CuMnAs. Lower right: Mn d-orbital projected band structure of c-axis AFM CuMnAs.

### 5.1.1 Projected band structure of c-axis AFM CuMnAs

I use a homemade python code to do the projected band for non-colinear calculation. The bandwidth is proportional to the value of the projected weight  $|\langle Y_{lm}^{\alpha} | \phi_{nk} \rangle|^2$  of that particular band index and crystal momentum. The spherical harmonic is centered at selected ion positions (ex. Mn here). The projected weight value is taken directly from PROCAR of the VASP calculation. In the lower right of figure 5.1 I show the projected band of the Mn-d orbital which is the most dominating orbital near the Fermi level. This not only makes the Wannier fitting easier but also allows us to understand what orbital should we think of as a simplified model of this material.



### 5.1.2 Density of states of c-axis AFM CuMnAs

In the lower left of figure 5.1 I show the partial density of states. As is clear in the plot, c-axis AFM CuMnAs is a semimetal with Mn d-orbital and Cu d-orbital dominating around the Fermi level. The most dominant orbitals are the d-orbitals of Mn, we can approximate the material to only consists of this orbital to do the analysis regarding low-energy excitations. Also, we notice Mn is also the atom with a local AFM structure, so the change of local magnetic direction is supposed to affect bands near the Fermi level.

Next, we show some supplement plots to add clarity. The Wannier band is fit up to a full gap along this high symmetry line. The two bands here are almost identical and the fitted energy range allows us to study the optical properties in our region of interest. On the right of figure 5.2 we can see the original Dirac point gapped out due to lack of  $S_{2z}$  and the soc gaps remain open. We can also use IRVASP [38] to let irreducible representations to determine if the bands are crossing or not [39].

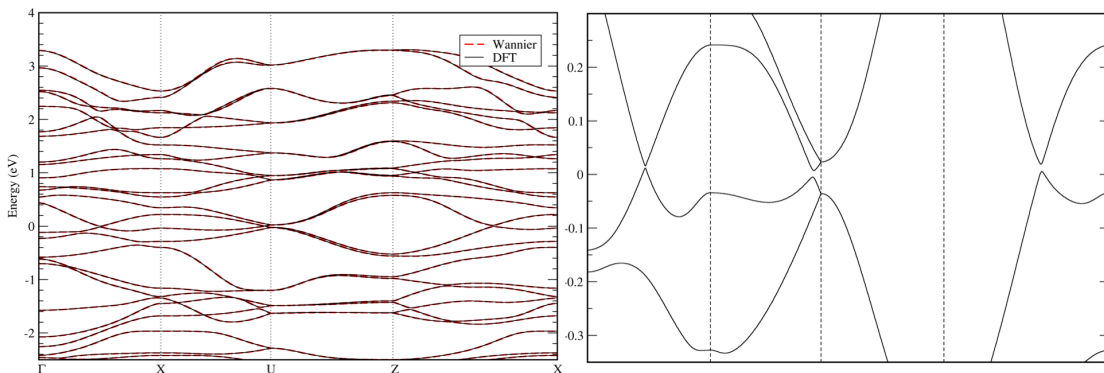


Figure 5.2: Left: Wannier and DFT band up to the full gap. Right: zoom in view of the b-axis CuMnAs band, it is gapped for all three energetically close points.

The b-axis AFM CuMnAs still possess PT-symmetry but break the  $S_{2z}$  symmetry that protects the Dirac point from being split by spin-orbit interaction. This is the main difference that can be seen in the band structure while other properties mentioned before in the c-axis AFM CuMnAs band structure remain roughly the same.



## 5.2 Joint density of states and linear optical conductivity of c-axis and b-axis AFM CuMnAs

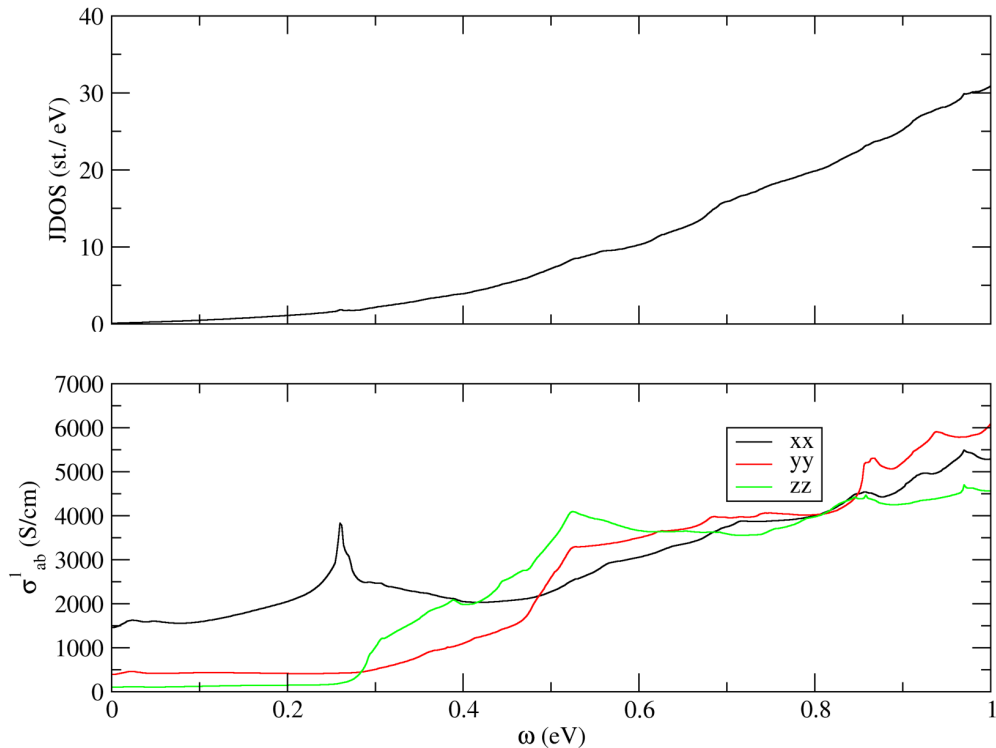


Figure 5.3: Joint density of states and first-order optical conductivity of c-axis AFM CuMnAs.

We observe a small but relatively sharp peak for  $\sigma_{xx}$  component around 0.26 eV that doesn't appear in the case of LaAlGe.

In b-axis AFM CuMnAs, the first-order optical conductivity has a large peak at low energy region, especially for the  $\sigma_{yy}$  component. So the second-order conductivity peak may be due to this already large transition amplitude in the first-order perturbation. As the second-order conductivity can be viewed as a product of transition amplitude times the shift of electron position or the change of electron velocity for shift and injection respectively.

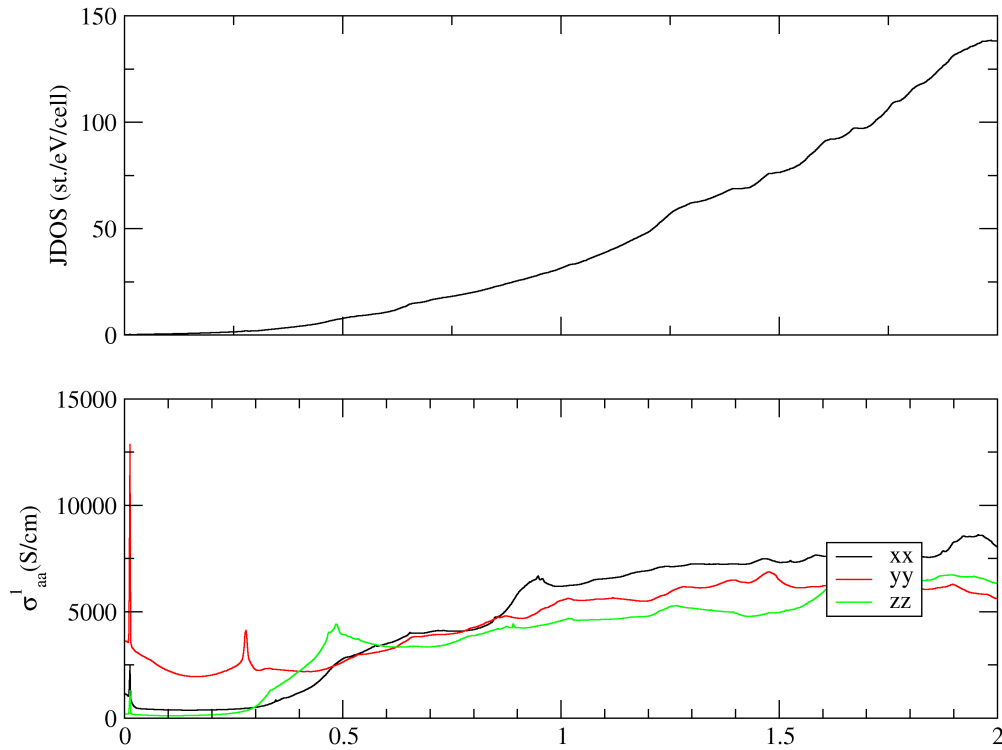
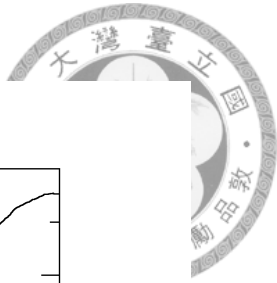


Figure 5.4: Joint density of states and first-order optical conductivity of b-axis AFM CuMnAs.

### 5.3 Shift and injection current conductivity spectrum for c-axis and b-axis AFM CuMnAs

For both the c-axis and b-axis AFM CuMnAs, the nonzero currents are linear injection and circular shift currents from the symmetry analysis. Below we will also list only the nonzero components of the correspondent conductivity spectrum. Different from the case of LaAlGe, since the energy of the Dirac point in c-axis AFM CuMnAs is extremely close to the Fermi level, I will show here only the results of setting the Fermi energy as the self-consistent calculation result.

We observe a plus-minus oscillating behavior in all components of the linear injection current in c-axis CuMnAs. The dominating component is  $\sigma_{yxz}$  where the oscillating pattern is even more clear and the magnitude of the peaks decrease roughly exponentially as



the frequency increase.

Via symmetry analysis, we know the c-axis AFM CuMnAs have the same nonzero components for linear injection and circular shift current. Yet we can use the magnitude to separate them. As can be seen from the above plot, circular shift current is dominated by  $\sigma_{xyz}$   $\sigma_{zxy}$  components while linear injection current is by  $\sigma_{yxz}$ . We also observe similar oscillating behavior in the circular shift current spectrum and while symmetry analysis didn't predict any relation between these independent components, in both of the above conductivities,  $\sigma_{xyz}$  and  $\sigma_{zxy}$  component seemed dependent (they are roughly the same for linear injection and posses opposite sign in circular shift current). The b-axis AFM CuMnAs have the same nonzero currents as c-axis AFM CuMnAs due to the fact that they both process PT-symmetry and break time-reversal symmetry. So we will be interested in comparing the magnitude of these currents (they may also be of different nonzero components due to their different magnetic space groups). We notice the  $\sigma_{xyy}$  component is dominating in magnitude for linear injection current in b-axis AFM CuMnAs. Yet the magnitude is roughly 2/3 smaller than the c-axis AFM CuMnAs linear injection current. And there is no oscillating behavior for the b-axis AFM CuMnAs.

For circular shift current of b-axis CuMnAs, it has also one particular component dominating the rest, namely the  $\sigma_{xyy}$  component. It is roughly of the same magnitude as that of the c-axis AFM CuMnAs. The fact that there is also no oscillation pattern in the case of b-axis CuMnAs is intriguing and I will further compare the contributions along high symmetry  $k$ -path of the oscillating and non-oscillating distinction between c-axis and b-axis CuMnAs.

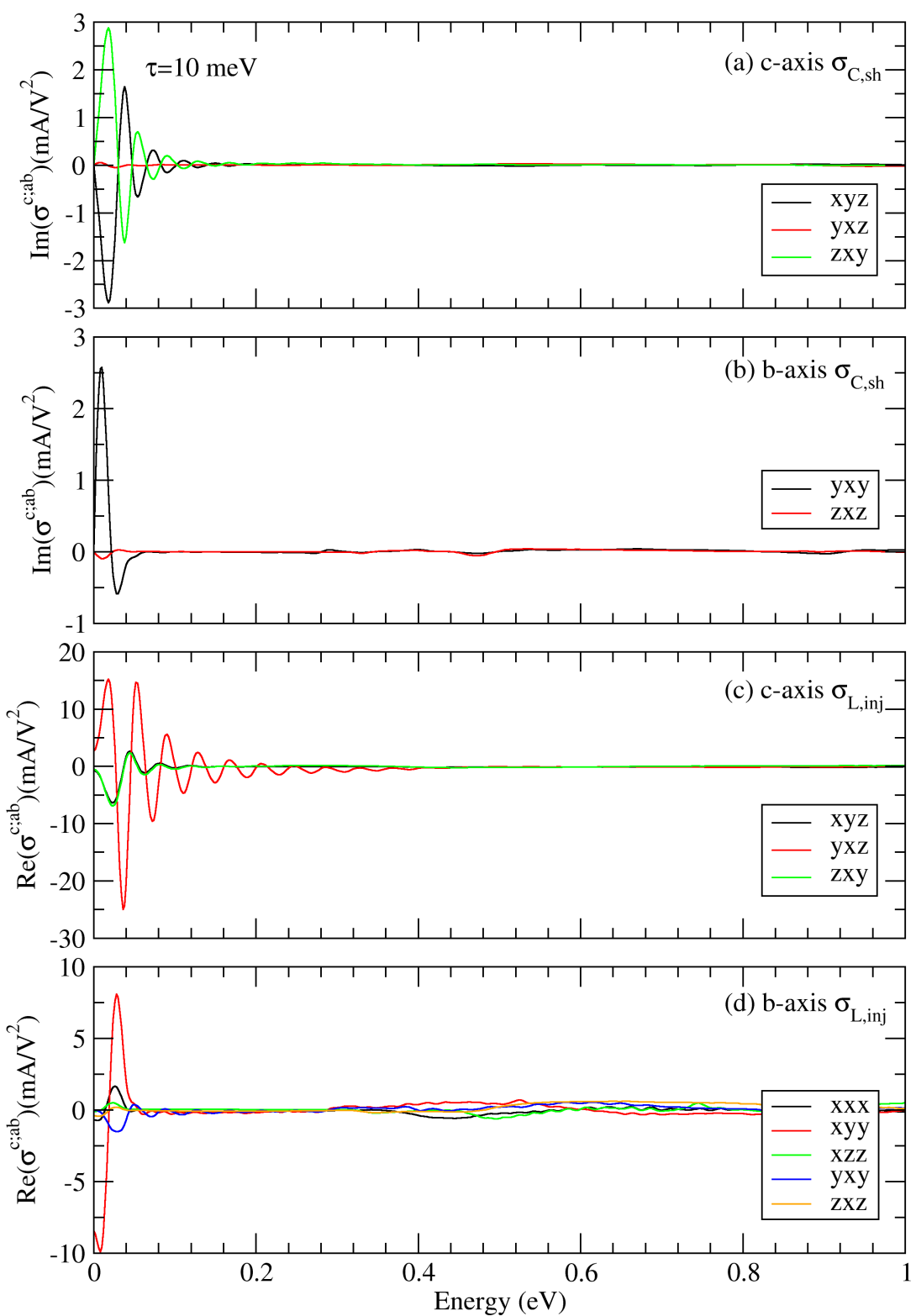
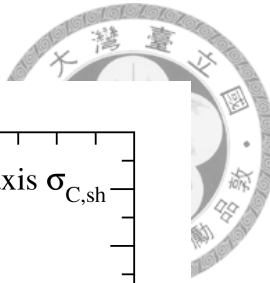


Figure 5.5: Independent component of linear injection and circular shift current in c-axis and b-axis AFM CuMnAs. (a) circular shift current of c-axis AFM CuMnAs, (b) circular shift current of b-axis AFM CuMnAs, (c) linear injection current of c-axis AFM CuMnAs, (d) linear injection current of b-axis AFM CuMnAs.



## 5.4 $k$ -path analysis of circular shift current and Christoffel symbol of the first kind of c-axis and b-axis AFM CuMnAs

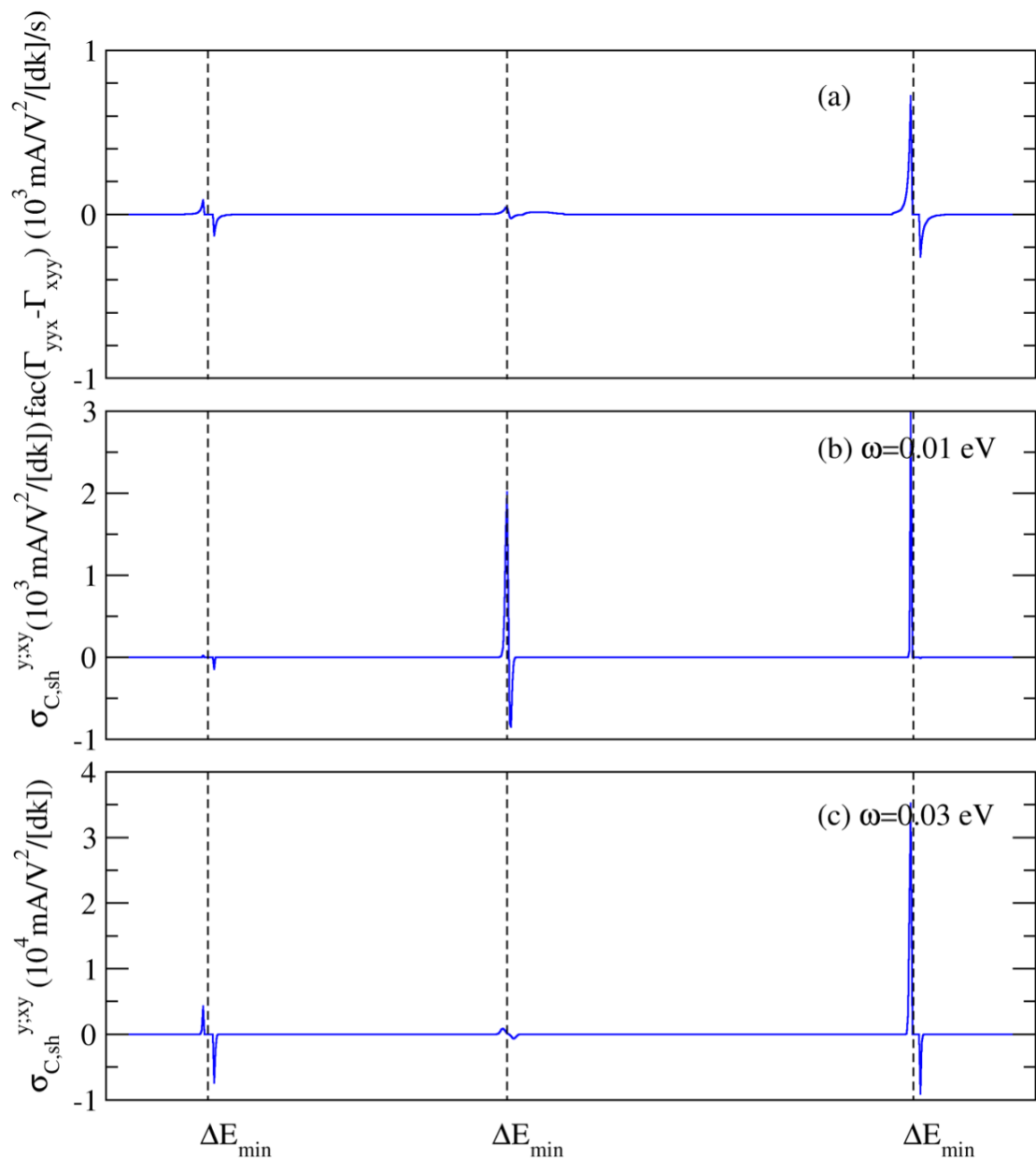


Figure 5.6:  $k$ -path of circular shift conductivity and Christoffel symbol of the first kind ( $\Gamma$ ) in b-axis CuMnAs. The  $k$ -path is the same high symmetry path used for drawing band structure, and  $\Delta E_{min}$  is the  $k$ -point where the two gapped-out Dirac bands have the smallest energy difference. (a) Difference of Christoffel symbols of the first kind with  $fac = \pi e^3 / 2\hbar^2$ . (b) Circular shift current with peak energy 0.01 eV. and (c) 0.03eV.

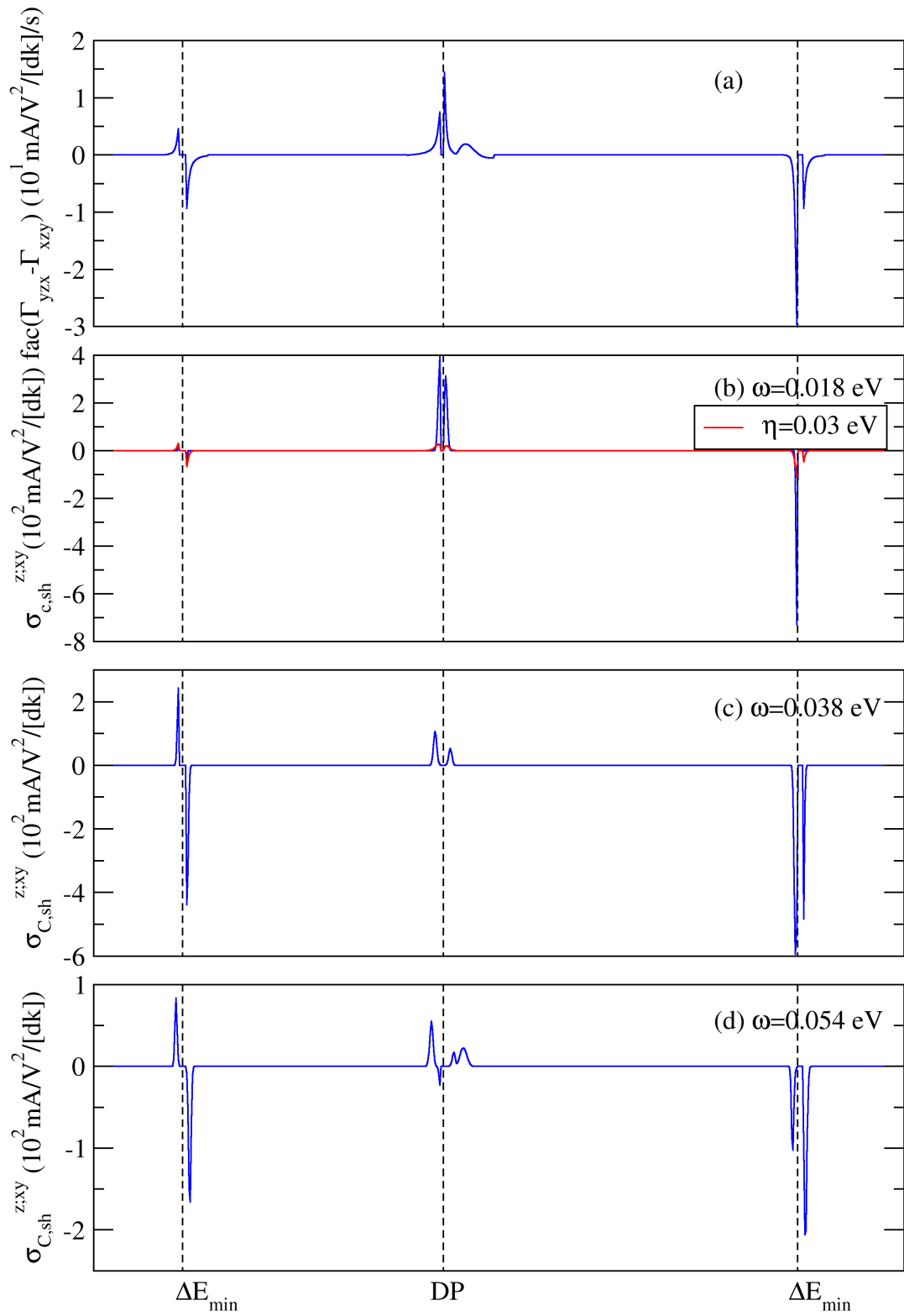
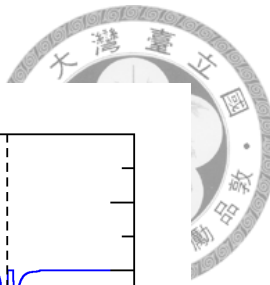
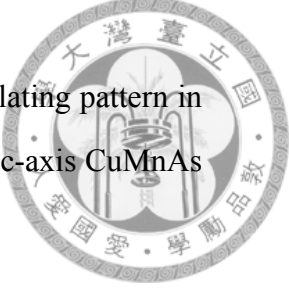


Figure 5.7:  $k$ -path of circular shift conductivity and Christoffel symbol of the first kind ( $\Gamma$ ) in c-axis CuMnAs. The  $k$ -path is the same high symmetry path used for drawing band structure,  $\Delta E_{\min}$  is the  $k$ -point where the two gapped-out Dirac bands have the smallest energy difference, and DP is the Dirac point. (a) Difference of Christoffel symbols of the first kind with  $\text{fac} = \pi e^3 / 2\hbar^2$ . (b) Circular shift current with peak energy 0.018 eV, (c) 0.038eV, and (d) 0.052 eV.



In order to understand the origin of circular shift current and (non-)oscillating pattern in (b-) and c-axis CuMnAs, I choose  $\sigma_{yxy}$  for b-axis CuMnAs and  $\sigma_{zxy}$  for c-axis CuMnAs to study. According to [31], the shift current can be expressed as

$$\sigma_{shift}^{c;ab} = -\frac{\pi e^3}{2\hbar^2} \sum_{n,m} \int_k \delta(\omega - \omega_{mn}) f_{nm} i (C_{bca}^{mn} - (C_{acb}^{mn})^*) , \quad (5.1)$$

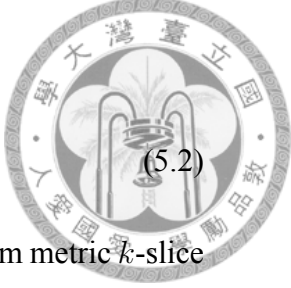
with  $C_{bca}^{mn} = r_{nm}^b r_{mn,c}^a$ , and the real part of  $C_{bca}^{mn}$  is the metric connection. From figure 5.6 we see the Christoffel symbol of the first kind is clear near  $\Delta E_{min}$  with one positive peak on the left and one positive peak on the right. Also, the peak is very concentrated around  $\Delta E_{min}$ , so when different incident photon energies pick up different parts of  $\Gamma$ , it decreases fast without sign of oscillation.

On the other hand, from figure 5.7 we see the Christoffel symbol of the first kind has multiple peaks, a more diverged peak shape, and is more spread near DP and  $\Delta E_{min}$ . As a consequence, when different incident photon energies pick up different parts of  $\Gamma$ , it can oscillate in sign and the magnitude is much larger for the following peaks compare to that of b-axis CuMnAs.

## 5.5 *k*-slice analysis of linear injection conductivity and quantum metric of c-axis and b-axis AFM CuMnAs

For c-axis AFM CuMnAs we seek the connection between the Dirac point on X-U, linear injection spectrum, linear injection conductivity *k*-slice, and quantum metric *k*-slice. We found a similar scenario happening again with a twist of the Fermi surface contour taking a close concentric oval shape in the case of c-axis AFM CuMnAs. Another difference is in the Dirac point structure: there are no different (sets) of Dirac points located at different energy in the Brillouin zone and the two Fermi surfaces are close in *k*-space distance causing the dominant region centered around the Fermi surface rather than the Dirac point itself.

We make a similar analysis as in the case of LaAlGe. Now we take the *Re* part of the



two-band formula

$$\sigma_{inj,L}^{c;ab} = -\tau \frac{2\pi e^3}{\hbar^2} \int_{\omega=\omega_{cv}} \frac{d^{d-1}k}{(2\pi)^d} (\hat{n} \cdot \hat{c}) g_{ba},$$

where  $g_{ba}$  is the quantum metric. We see again the (a)symmetry of quantum metric  $k$ -slice change correspondingly according to the current direction. Take the  $\sigma_{xyz}$  component of the linear injection, for example, the current direction is along the x-axis so the quantum metric is asymmetric under  $M_x$  for both the outer and inner Fermi surface. And since the outer and inner Fermi surfaces possess opposite  $\hat{n}$  surface normal directions (they have opposite  $\nabla E$ ), the quantum metric should also change sign for each outer-inner pair (see upper left figure).

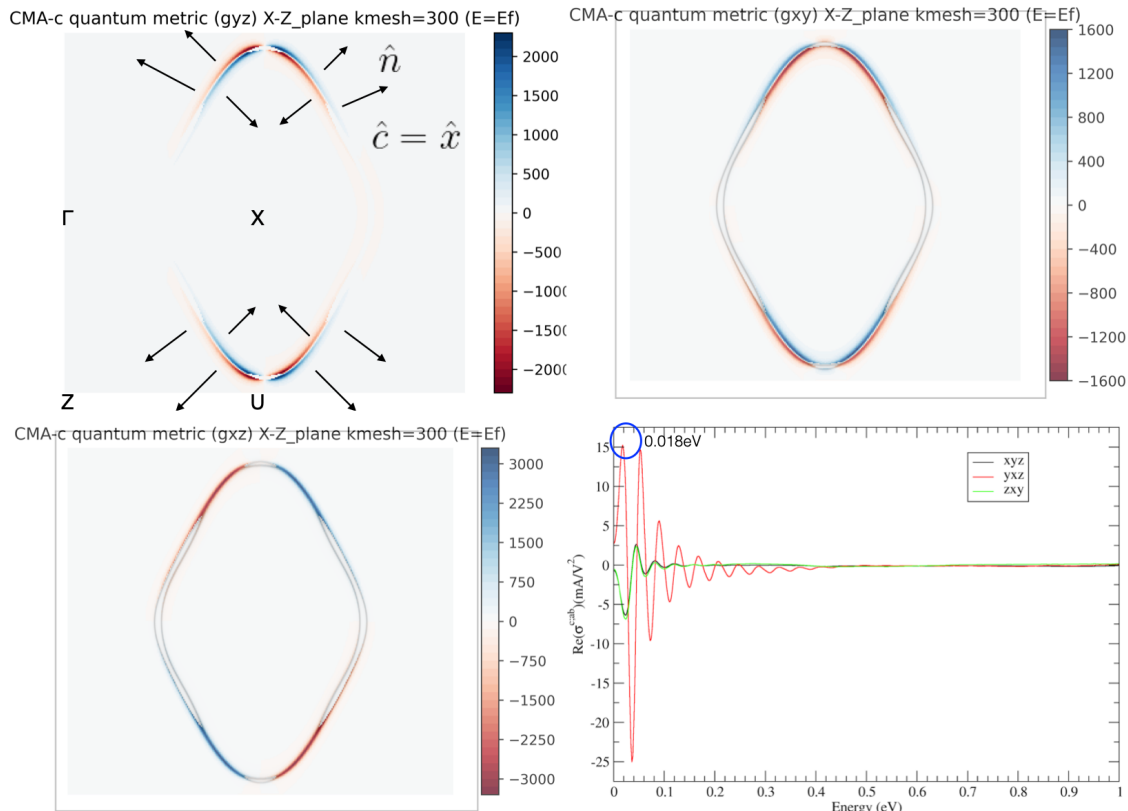


Figure 5.8: Quantum metric  $k$ -slice on X-Z plane containing  $\Gamma$  point and linear injection spectrum of c-axis AFM CuMnAs. Upper left:  $g_{yz}$ ; Upper right:  $g_{xy}$ , the grey contour is the Fermi surface; bottom left:  $g_{xz}$ ; bottom right: linear injection spectrum.

For the b-axis AFM CuMnAs, the dominating linear injection component is  $\sigma_{xyy}$  and we notice two things. First, the most contributed regions in the Brillouin zone are not around the two close Fermi surfaces, it sits right on and near the blurry lines that represent states energetically close to but not exactly on the Fermi surface. The other is that the



quantum metric has no asymmetry in the Brillouin zone, it has the same sign across all Brillouin zone. If we compare the quantum metric  $k$ -slice and Fermi surface of the most dominating component of linear injection for c- and b-axis AFM CuMnAs, we see that they both sit right at and near the blurry line instead of near the sharp lines of the Fermi level. The (a)symmetry is rather puzzling for both c-axis and b-axis AFM CuMnAs in figure 5.9. For the c-axis AFM CuMnAs, it may be due to the fact that the current direction ( $\hat{y}$ ) is perpendicular to the  $k$ -slice plotted here so we can no longer use the previous analysis to analyze. As for b-axis AFM CuMnAs, we notice the dominating regions are not split like the case of  $g_{yz}$  and  $g_{xy}$  in c-axis AFM CuMnAs. Why some of the components are dominant in energetically closed and split contours while others concentrate on one oval contour requires more detailed analysis. It seems whenever the dominant regions are split contours, the asymmetric rule mentioned previously holds.

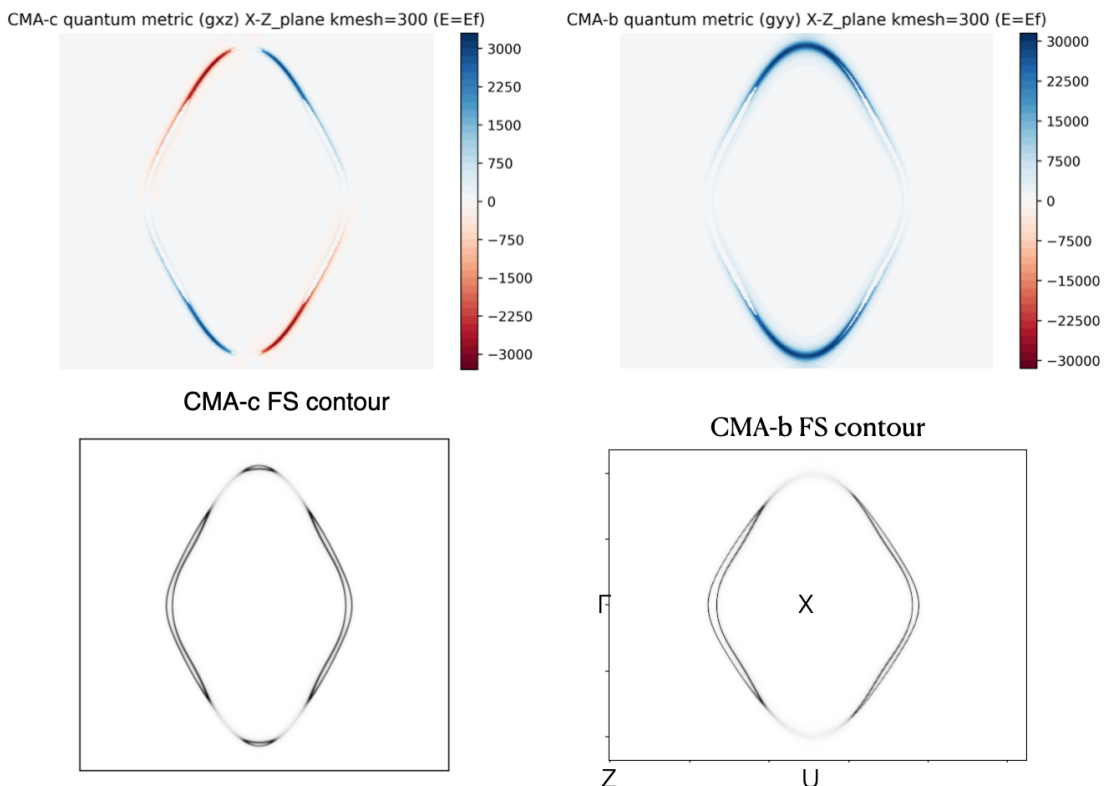


Figure 5.9: Quantum metric and Fermi surface contour  $k$ -slice on X-Z plane containing  $\Gamma$  point. Left: c-axis AFM CuMnAs; right: b-axis AFM CuMnAs.



# Chapter 6

## Conclusion

In conclusion, this thesis provides a detailed derivation and explanation of bulk photovoltaic effect and quantum geometries based on the work of previous papers [1][2]. After the theoretical background is presented, we choose two materials to do the first principle studies. An introduction of the current state of research is given followed by their physical properties. Electronic structures and first-order optical conductivity are calculated to support theoretical analysis of the bulk photovoltaic effect. The spectrums of shift and injection current are calculated followed by the  $k$ -slice analysis which looks at contributions inside the Brillouin zone.

The two materials, nonmagnetic Weyl semimetal LaAlGe and antiferromagnetic Dirac semimetal CuMnAs, complete all the BPVE currents and their corresponding geometric quantities. For BPVE and its quantum geometries, Wannier functions and Kohn-Sham orbitals obtained from first-principle density functional theory are used for the calculations. I also try to find out dominant regions and possible mechanisms for various quantities.

A large circular injection current close to  $20 \text{ mA/V}^2$  and linear shift current up to  $0.5 \text{ mA/V}^2$  is calculated in LaAlGe. Component change and a clear peak emerge for the linear injection current in CuMnAs when the local magnetic moment direction is changed from the c-axis to the b-axis.

All the bulk photovoltaic effects and quantum geometric quantities are systematically studied in LaAlGe, c-axis AFM CuMnAs, and b-axis AFM CuMnAs. Furthermore, the  $k$ -slice study of the quantum metric shows interesting asymmetry behavior directly corre-



sponding to the outgoing current direction.

This thesis serves as a starting point for analyzing photovoltaic effects and quantum geometric quantities in real materials using first principle method. Directions of future work include further explanations of the sign change mechanism in the spectrum when we shift the chemical potential. Another direction is to try to find other quantized quantities from these geometric relations.



# Bibliography

- [1] C. Aversa and J. E. Sipe, Nonlinear optical susceptibilities of semiconductors: Results with a length-gauge analysis, *Phys. Rev. B.* **52**, 14636 (1995).
- [2] J. Ahn, G.-Y. Guo, and N. Nagaosa, Low-Frequency Divergence and Quantum Geometry of the Bulk Photovoltaic Effect in Topological Semimetals, *Phys. Rev. X.* **10**, 041041 (2020).
- [3] M. Kawasaki, (2019). Topological shift current [PowerPoint slides]. Department of Applied Physics, University of Tokyo. <https://indico.ictp.it/event/8727/session/48/contribution/164/material/slides/0.pdf>
- [4] N. P. Armitage, E. J. Mele, and A. Vishwanath, Weyl and Dirac semimetals in three-dimensional solids, *Rev. Mod. Phys.* **90**, 015001 (2018).
- [5] H. Weyl, Gravitation and the electron, *Proc. Natl. Acad. Sci. U.S.A.* **15**, 323 (1929).
- [6] M.-C. Chang, Lecture notes on topological insulators (2017).
- [7] M. V. Berry, Aspects of Degeneracy, Springer, (1985).
- [8] D. Xiao, M.-C. Chang, Q. Niu, Berry phase effects on electronic properties, *Rev. Mod. Phys.* **82**, 1959 (2010).
- [9] Z. Ni, K. Wang, Y. Zhang, O. Pozo, B. Xu, X. Han, K. Manna, J. Paglione, C. Felser, A. G. Grushin, F. de Juan, E. J. Mele, and L. Wu, Giant topological longitudinal circular photo-galvanic effect in the chiral multifold semimetal CoSi, *Nat. Commun* **12**, 154 (2021).



- [10] S. M. Girvin and K. Yang, Modern Condensed Matter Physics. 1, Cambridge University Press, (2019).
- [11] E. I. Blount, Solid State Physics. 1, Elsevier, (1962).
- [12] Y. Guo, H. Zhu, and Q. Wang, Large Second Harmonic Generation in Elemental  $\alpha$ -Sb and  $\alpha$ -Bi Monolayers, J. Phys. Chem. C **124**, 5506 (2020).
- [13] H. T. Stokes, D. M. Hatch, and B. J. Campbell, FINDSYM, ISOTROPY Software Suite, iso.byu.edu.
- [14] H. T. Stokes and D. M. Hatch, FINDSYM: Program for Identifying the Space Group Symmetry of a Crystal, J. Appl. Cryst. **38**, 237 (2005).
- [15] G. Pizzi, V. Vitale, R. Arita, S. Blügel, F. Freimuth, G. Géranton, M. Gibertini, D. Gresch, C. Johnson, T. Koretsune, J. Ibañez-Azpiroz, H. Lee, J. M. Lihm, D. Marchand, A. Marrazzo, Y. Mokrousov, J. I. Mustafa, Y. Nohara, Y. Nomura, L. Paulatto, S. Poncé, T. Ponweiser, J. Qiao, F. Thöle, S. S. Tsirkin, M. Wierzbowska, N. Marzari, D. Vanderbilt, I. Souza, A. A. Mostofi, and J. R. Yates, Wannier90 as a community code: new features and applications, J. Phys. Cond. Matt. **32**, 165902 (2020).
- [16] B. Schutz, A First Course in General Relativity. 2, Cambridge University Press, (2009).
- [17] P. Hohenberg and W. Kohn, Inhomogeneous Electron Gas, Phys. Rev. **136**, B864 (1964).
- [18] W. Kohn, and L. J. Sham, Self-Consistent Equations Including Exchange and Correlation Effects, Phys. Rev. **140**, A1133 (1965).
- [19] A. Zee, Group Theory in a Nutshell for Physicists. 1, Princeton University Press, (2016).
- [20] C. Kittel, Introduction to Solid State Physics. 8, Wiley, (2004).
- [21] G. Grossi and G. P. Parravicini, Solid State Physics. 2, Elsevier, (2014).



- [22] G. Kresse and J. Hafner, *Ab initio* molecular dynamics for liquid metals, *Phys. Rev. B* **47**, 558 (1993).
- [23] P. E. Blöchl, Projector augmented-wave method, *Phys. Rev. B* **50**, 17953 (1994).
- [24] J. P. Perdew, K. Burke, and M. Ernzerhof, Generalized Gradient Approximation Made Simple, *Phys. Rev. Lett.* **77**, 3865 (1996).
- [25] A. M. Guloy, J. D. Corbett, Syntheses and structures of lanthanum germanide,  $\text{LaGe}_{2-x}$ , and lanthanum aluminum germanide,  $\text{LaAlGe}$ : interrelationships among the  $\alpha\text{-ThSi}_2$ ,  $\alpha\text{-GdSi}_2$ , and  $\text{LaPtSi}$  structure types, *Inorg. Chem.* **30**, 4789 (1991).
- [26] J. T. Zhao and E. Parthe, Structure of YAI<sub>Ge</sub> and Isotypic Rare-Earth-Aluminium Germanides, *Acta Cryst. C* **46**, 2276 (1990).
- [27] J. Mündelein and H.-U. Schuster, Preparation and crystal structure of compounds  $\text{MnCuX}$  ( $\text{X}=\text{P, As, P}_x\text{As}_{1-x}$ ), *Z. Naturforsch. B* **47**, 925 (1992).
- [28] P. E. Blöchl, O. Jepsen, and O. K. Andersen, Improved tetrahedron method for Brillouin-zone integrations, *Phys. Rev. B* **49**, 16223 (1994).
- [29] J. Ibañez-Azpiroz, S. S. Tsirkin, and I. Souza, Ab initio calculation of the shift photocurrent by Wannier interpolation, *Phys. Rev. B* **97**, 245143 (2018).
- [30] X. Wang, J. R. Yates, I. Souza, and D. Vanderbilt, *Ab initio* calculation of the anomalous Hall conductivity by Wannier interpolation, *Phys. Rev. B* **74**, 195118 (2006).
- [31] J. Ahn, G.-Y. Guo, N. Nagaosa, and A. Vishwanath, Riemannian geometry of resonant optical responses, *Nat. Phys.* **18**, 290 (2022).
- [32] S.-Y. Xu, N. Alidoust, G. Chang, H. Lu, B. Singh, I. Belopolski, D. S. Sanchez, X. Zhang, G. Bian, H. Zheng, M.-A. Husanu, Y. Bian, S.-M. Huang, C.-H. Hsu, T.-R. Chang, H.-T. Jeng, A. Bansil, T. Neupert, V. N. Strocov, H. Lin, S. Jia, M. Z. Hasan, Discovery of Lorentz-violating type II Weyl fermions in LaAlGe, *Sci. Adv.* **3**, e1603266 (2017).



- [33] G. Chang, B. Singh, S.-Y. Xu, G. Bian, S.-M. Huang, C.-H. Hsu, I. Belopolski, N. Alidoust, D. S. Sanchez, H. Zheng, H. Lu, X. Zhang, Y. Bian, T.-R. Chang, H.-T. Jeng, A. Bansil, H. Hsu, S. Jia, T. Neupert, H. Lin, and M. Z. Hasan, Magnetic and noncentrosymmetric Weyl fermion semimetals in the RAlGe family of compounds (R = rare earth), *Phys. Rev. B* **97**, 041104 (2018).
- [34] F. Maca, J. Masek, O. Stelmakhovych, X. Marti, H. Reichlova, K. Uhlirova, P. Bezan, P. Wadley, V. Novak, and T. Jungwirth, Room-temperature antiferromagnetism in CuMnAs, *J. Magn. Magn. Mater.* **324**, 1606 (2012).
- [35] P. Tang, Q. Zhou, G. Xu, and S.-C. Zhang, Dirac fermions in an antiferromagnetic semimetal, *Nat. Phys.* **12**, 1100 (2016).
- [36] E. Emmanouilidou, H. Cao, P. Tang, X. Gui, C. Hu, B. Shen, J. Wu, S.-C. Zhang, W. Xie, and N. Ni, Magnetic order induces symmetry breaking in the single-crystalline orthorhombic CuMnAs semimetal, *Phys. Rev. B* **96**, 224405 (2017).
- [37] Q. Wu, S. Zhang, H.-F. Song, M. Troyer, and A. A. Soluyanov, WannierTools: An open-source software package for novel topological materials, *Comput. Phys. Commun.* **224**, 405 (2018).
- [38] J. Gao, Q. Wu, C. Persson, and Z. Wang, Irvsp: to obtain irreducible representations of electronic states in the VASP, arXiv 2002.04032 (2020).
- [39] M. S. Dresselhaus, G. Dresselhaus, and A. Jorio, *Group Theory Applications to the Physics of Condensed Matter*. 1, Springer, (2008).